High Order Sonic Boom Modeling by Adaptive Methods

Frédéric Alauzet, Adrien Loseille

INSTITUT NATIONAL DE RECHERCHE EN INFORMATIQUE ET EN AUTOMATIQUE

High Order Sonic Boom Modeling by Adaptive Methods

Frédéric Alauzet — Adrien Loseille

N° 6845

February 19, 2009

Thème NUM

ISSN 0249-6399 ISRN INRIA/RR--6845--FR+ENG

High Order Sonic Boom Modeling by Adaptive Methods

Frédéric Alauzet*, Adrien Loseille†

Thème NUM — Systèmes numériques
Projet Gamma

Rapport de recherche n° 6845 — February 19, 2009 — 54 pages

Abstract: This report presents an accurate approach to simulate the sonic boom of a supersonic aircraft. The near-field flow is modeled by the conservative Euler equations and is solved using a vertex-centered finite volume approach on adapted unstructured tetrahedral meshes. Then, from the CFD solution, the pressure distribution under the aircraft is extracted and used to set up the initial conditions of the propagation algorithm in the far-field. The pressure distribution is propagated down to the ground in order to obtain the sonic boom signature using a ray tracing algorithm based upon the Thomas waveform parameter method. In this study, a sonic boom sensitivity analysis on several aircraft geometries is carried out.

Key-words: Sonic boom, Euler equations, finite volume, anisotropic mesh adaptation, Waveform Parameter Method.

* Email : Frederic.Alauzet@inria.fr
† Email : Adrien.Loseille@inria.fr

Unité de recherche INRIA Rocquencourt
Domaine de Voluceau, Rocquencourt, BP 105, 78153 Le Chesnay Cedex (France)
Téléphone : +33 1 39 63 55 11 — Télécopie : +33 1 39 63 53 30

Modélisation d'ordre élevée du bang sonique par des méthodes adaptatives

Résumé : Ce rapport présente une approche précise pour simuler le bang sonique emis par un avion supersonique. Le champ proche, *i.e.,* près de l'avion, est modélisé par les équations d'Euler conservative. Elles sont résolues par une méthode de volumes finis sur des maillages adaptés tétraédriques. Ensuite, à partir de cette solution, une distribution de pression est extraite sous l'avion. Elle est utilisée pour définir les conditions initiales de l'algorithme de propagation dans le champ lointain, *i.e.,* l'atmosphère. La distribution de pression est propagée jusqu'au sol en utilisant un algorithme de tracé de rayon basé sur la méthode des paramètres de forme de Thomas. On obtient alors la signature de bang sonique de l'avion. Dans cette étude, une analyse de sensibilité du bang sonique sera réalisée sur plusieurs géométries d'avion.

Mots-clés : Bang sonique, équations d'Euler, volumes finis, adaptation de maillage anisotrope, méthode des paramètres de formes.

1 Introduction

The sonic boom is an acoustic phenomenon associated to bodies moving in the atmosphere at a speed exceeding the local speed of sound. When an aircraft exceeds the speed of sound, shock waves are generated at its surface and emanate outward, forming the Mach cone, see Figure 2. Usually, these shock waves coalesce into a characteristic N shape wave when they propagate in the atmosphere toward the ground. The "boom-boom" heard on the ground comes from the abrupt pressure increase in the ambient air, *i.e.,* the two shock waves of the N shape acoustic signal. The region exposed to the sonic boom horizontally extends on each side of the aircraft path on the ground on a band of 60 to 80 kilometers width depending on flight conditions, see Figure 3. As a result, the sonic boom of supersonic aircrafts has a major impact on the environment: annoyance for populations due to noise and startle, but also rattles and vibrations on buildings. At worst, the latter phenomenon can break windows and damage buildings. For instance, the Concorde, that flew from 1969 to 2003, was allowed to fly supersonically only over water because its boom annoyed people on the ground. For this reason, the most of the current national regulation does not allow any supersonic flight over land.

Nonetheless, there is nowadays a substantial economical interest in designing a low sonic boom supersonic business jet in order to respect this environmental constraint. Indeed, if we consider a flight in the US from New York to Los Angeles, the travel time can be divided by two while flying at a supersonic cruise speed instead of a subsonic one. The main problem is that there is no conventional shape to reduce the boom. However, it has been stated that significant reduction in the shock overpressure levels is achieved by reducing the size, *i.e.,* the weight [29]. Consequently, focussing on business jets would be the first step. Several companies all around the world are thus involved in several research programs in order to propose low boom shape supersonic business jet.

In this context, numerical simulation faces a challenging problem. As constructing prototype is very (too) expensive, this is the way coupled with wind-tunnel testing to design low boom aircraft shape. To this end, shape optimization methods, that are now mature, are employed. But, the optimization process converges toward the best low boom shape if the sensitivity function is accurately evaluated. As a result, numerical methods must have the ability to assess sonic booms they compute for a given shape. It ensures that the direction of the gradient descent is not due to numerical artifacts. High-fidelity numerical predictions of sonic boom are then of main interest in designing low sonic boom aircraft configurations.

Modeling the sonic boom. The main difficulty in high-fidelity sonic boom numerical modeling lies in the large variations of the problem scales: they vary from the millimeter on the aircraft to the kilometer in the atmosphere. But nowadays, considering the ever increasing computational power available, such high-fidelity predictions become conceivable. Indeed, fairly simple methods based on linear theories were used in the past to predict sonic booms, such as [4]. Today, methods coupling CFD, that enables accurate non-linear near-field solutions around aircraft, with linear acoustics for propagation in the atmosphere toward the ground are available [27, 30]. More precisely, the flow close to the aircraft, called aerodynamic near-field region, is computed by solving the conservative Euler equations for gas dynamic. Then, from the CFD solution, the pressure distribution under the

aircraft is extracted and used to set up the initial conditions for the propagation algorithm in far-field. The pressure distribution is then propagated down to the ground to compute the sonic boom signature using linear acoustic.

The main problematic with these coupled methods is that some assumptions are required to ensure a valid coupling. As stated in [30], there is a matching radius between the source function and the propagation extrapolation. The assumption is that the use of the pressure signal become valid when the flow field does no more contain any crossflow components. As crossflow components are very significant at small radii but are less at larger distances. The pressure signal has to be extracted in the mid-field far enough from the aircraft to respect such condition. This is a necessary condition to take all the elements of the aircraft geometry (body, wings, engine,...) into account.

Present status. Standard CFD is only able to attain at most a distance below the jet of one aircraft length which is not enough to validate the coupling. After this distance, the solution is completely dissipated and the signal is lost. Consequently, new three-stage methods have been developed. One method considers a coupling between CFD, a multi-pole based near field reconstruction to take into account crossflow components [14] and linear propagation [31]. Another approach would couple near-field, mid-field and far-field simulations, see for instance [38].

The methods cited above always require an accurate CFD computation. If this computation is not valid, *i.e.,* not enough accurate, then the sonic boom prediction is not correct. In particular, these CFD computations employ isotropic unstructured meshes (to be able to handle complex aircraft geometries) that introduce a lot of numerical dissipation while propagating the shock waves. The consequence is that the near-field is generally not accurately predicted at a one aircraft length distance when the geometry is too complex. Certified CFD computation seems to be a necessity.

On the other hand, in the last decade, 3D meshing dedicated to CFD has tremendously progressed with notably the advent of anisotropic mesh adaptation. This technique has already proved its efficiency to reduce drastically the require number of degrees of freedom to achieve a given complexity [6, 12, 16, 23, 28, 36]. Furthermore, anisotropic mesh adaptation reduces particularly the numerical dissipation of shock capturing schemes and recovers the numerical scheme convergence order that is generally lost for flows with genuine discontinuities [25]. In this paper, we propose an alternative two-stage approach based on adaptive CFD.

The proposed approach. A high-fidelity method to predict accurately the sonic boom emitted by supersonic aircrafts is discussed. This approach is fully automatic and thus immediately applicable whatever the aircraft geometry and whatever the flight conditions. It aims at:

- computing accurate CFD mid-field, *i.e.,* at a distance of the order of the kilometer from the aircraft. In particular, shock waves are kept separated in the mid-field and do not merge artificially due to any coarse mesh effect
- controlling the impact of the numerical dissipation of flow solvers on unstructured meshes. Shocks intensity are preserved, so as the non-linearities of the solution.

In our high-fidelity model, the resolution is two stepped, see Figure 1. The near-field and the mid-field flow are solved using a vertex-centered finite volume approach on adapted unstructured tetrahedral meshes. Adapted anisotropic mesh is utilized to break scale factors, leading to accurate near-field and mid-field predictions [12, 25].. The pressure distribution is then propagated down to the ground to compute the sonic boom signature using a ray tracing algorithm based upon the Thomas waveform parameter method [37].

It is important to note that this approach employs large CFD computations: dozens of millions of degrees of freedom for a simulation. For instance, simulations presented in this paper spent approximately half a week on 4 processors on 2 GHz frequency Mac Intel. Such simulations are performed to assess the sonic boom prediction. However, in this work, we point out that the numerical scheme obtained on anisotropic adapted meshes provides a consistent numerical dissipation. It results that even with smaller mesh size the sonic boom signal properties are preserved. Therefore, such method can be adapted to provide fast consistent answers.

In the present work, attention is paid on the coupling between the mid-field resolution and the far-field propagation. To resolve this issue, a convergence study of the sonic boom signature with respect to the extraction distance for the whole adaptive process is carried out.

In addition to the validity of the coupling, we aim at assessing the obtained numerical result as much as possible. We like to attest that the computed mid-field signature and the sonic boom signal converge toward the physical solution. In this paper, we show that anisotropic mesh adaptation

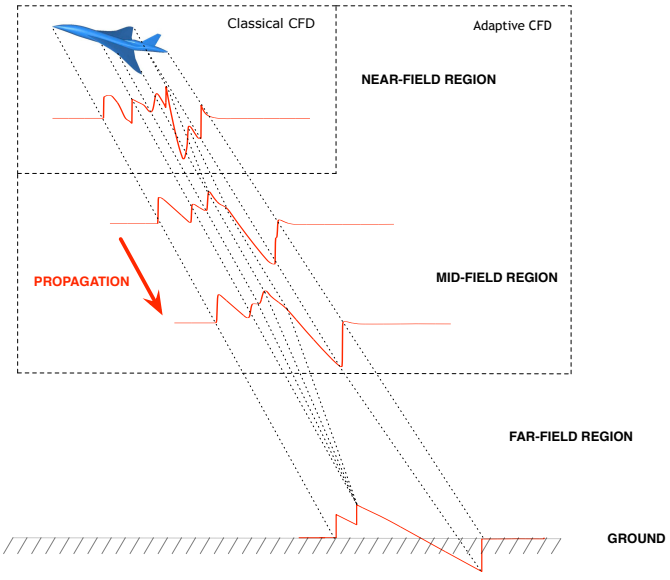

Figure 1: *Sonic boom problem modeling.*

helps to answer this question. Indeed, in order to be able to certify a result, the mesh convergence order of the numerical solution must be equal to the theoretical order of the numerical scheme. However, global second order of mesh convergence is generally scarcely reached for most practical application in which genuine discontinuities or sharp gradients are involved - and it is the case for the sonic boom problem. It has been demonstrated in [2] that anisotropic mesh adaptation enables to recover the theoretical convergence order. In broad outline, mesh adaptation strategy asks the mesh generator to add the number of required vertices in all regions to attain the theoretical convergence order.

Overview. In the following sections, we present our approach. The sonic boom physical phenomenon is recalled in Section 2. Section 3 details the CFD modeling. Section 3.1 describes the vertex-centered finite volume scheme used to compute near-field region flow and Section 3.2 recalls the mesh adaptation algorithm. We briefly review the main stages of the adaptation procedure. The CFD part is validated in Section 3.3 by comparison to experimental data. Then in Section 4, the ray tracing algorithm based upon the Thomas waveform parameter method is recalled and the coupling between the CFD and the propagation code is clarified. Finally, in Section 5, several aircraft shapes, provided by Dassault Aviation in the HISAC European project, are analyzed and compared. We eventually point out the impact of the anisotropic mesh adaptation to compute accurate mid-field signatures with CFD.

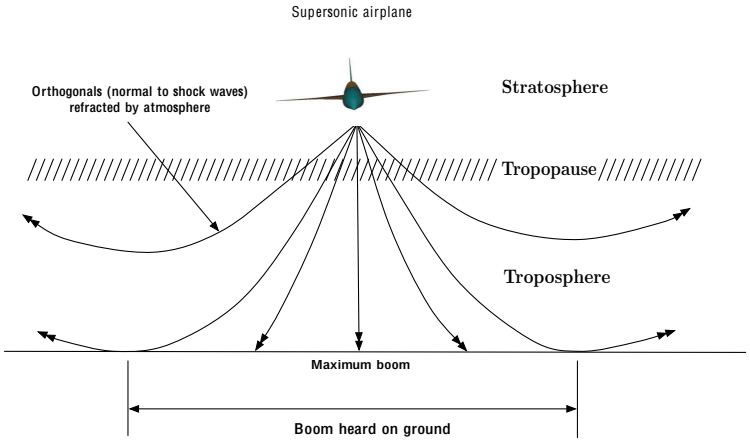

Figure 2: *Illustration of the sonic boom horizontal carpet with under the aircraft path and the refraction of acoustic waves by the atmosphere.*

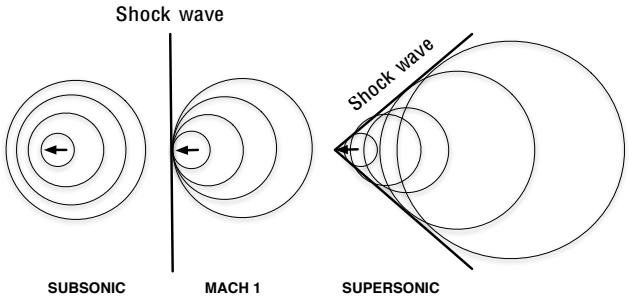

Figure 3: *Acoustic signal due to a moving object. When the object exceeds the speed of sound, the acoustic waves focalize into shock waves forming the Mach cone.*

2 Sonic boom: the physical phenomenon

The sonic boom, as every sound, corresponds to a small variation (positive for a compression or negative for an expansion) of the ambient air pressure with respect to the atmospheric pressure. This acoustic phenomenon is associated to bodies moving in the atmosphere at a speed exceeding the local speed of sound. This phenomenon is linked to the aircraft all along its supersonic flight and not only when the aircraft breaks the sound barrier. More precisely, a flying aircraft compresses the air creating surrounding acoustics over-pressure and under-pressure, cf. Figure 2, left. When the aircraft is moving at supersonic speed, the acoustic waves issued from it focalize inside a conic region forming shock waves. This region is the well known Mach cone, cf. Figure 2, right. It is a surface of discontinuity for most of the thermodynamic variables: pressure, density, velocity, entropy, ... The sound emitted by the aircraft is confined inside this cone. This cone has for vertex the aircraft nose and for half-angle α such that $\sin(\alpha) = c/a = M^{-1}$ where c, a and M are the sound speed, the aircraft velocity and the Mach number, respectively. Each part of the aircraft geometry emits its own Mach cone (nose, wings,...). However, these shocks waves propagate into the atmosphere at slightly different speed due to an over-pressure, which increases the air temperature thus accelerating the sound. For an aircraft, these shock waves propagate on enough large distance into the atmosphere (more than 10 km) to coalesce into a characteristic N shape wave. For this reason, we only heard the "boom-boom" on the ground due to the abrupt pressure increases in the ambient air, *i.e.,* the two shock waves of the N shape acoustic signal.

Nevertheless, the previous presentation is a simplified description of the sonic boom. The region exposed to the sonic boom horizontally extends on each side of the aircraft path on the ground on a band of 60 to 80 kilometers width depending on flight conditions, see Figure 3. This is the corridor where the sonic boom is heard called the primary carpet. In fact, the carpet width increases with the cruising altitude. In standard atmospheric conditions, temperature gradients curve the acoustic wave toward the top delimiting the carpet width. Generally, the acoustic signal in this primary carpet presents 2 shocks, the famous N shape, but sometimes more. Such sonic boom are created by cruising aircraft. The shapes of the wings and other lifting surfaces play a role in sculpting the sonic

boom signature. Cruising altitude is also a factor. If the aircraft flies higher then the shock waves have more time to coalesce into an N wave. The aircraft speed and the atmospheric conditions are also factors. Notice that in general, the maximum intensity of the sonic boom is reached in the area directly under the aircraft path and this intensity decreases progressively when we move away from the trajectory.

Moreover, aircraft maneuvers, such as acceleration, turning or diving, can lead to local amplification of the sonic boom. The signal shape is also considerably modified. The ground pressure signature generally take the shape of a U. Focalized sonic boom have positive shocks at the front and the rear of the signature where the intensity are higher that in standard N shape boom. The amplification coefficient factor can be of the order of 10 but it is localized in a small area. On the contrary, maneuvers such as deceleration or climbing can reduce the sonic boom. In this paper, we will only simulate sonic boom emitted by cruising aircraft.

The atmospheric variability has a major incidence on the sonic boom. In particular, wind, temperature and ground turbulence impact on one side the position and the size of the primary carpet and on the other side the shape and the intensity of the sonic boom. For instance, N shape wave can be transformed into U shape wave due to the atmospheric turbulence in the earth boundary layer. The rise time of the shocks is principally affected which has a large impact on our perception of the sonic boom.

As a result, the sonic boom of supersonic aircraft has a major impact on the environment. This impact is annoyance on populations due to noise and startle, but also rattles and vibrations on buildings. At the very worse, it can break windows and damage buildings cause by focalized boom. For instance, Concorde, that flew from 1969 to 2003, was allowed to fly supersonically only over water because its boom annoyed people on the ground. Over-pressure emitted by Concorde have an intensity of almost 100 Pa (2 psf). Consequently, there is an explicit prohibition of supersonic flight over lands under most of the current national regulation. To expect any change not only has the sonic boom to be suppressed, but public acceptance has also to be won. Right now, researches focus on developing a metric to judge whether the booms are acceptable or not.

Reducing the sonic boom. There is nowadays a substantial economical interest in designing a low sonic boom supersonic business jet in order to respect this environmental constraint. Indeed, if we consider a flight in the US from New York to Los Angeles of a distance $3\,930$ km. Then, a cruise speed of Mach 0.85 or 0.98 results in a flight of 5 hours or 4 hours and 20 minutes duration, respectively. Whereas a cruise speed of Mach 1.8 lead to a flight of only 2 hours and 15 minutes. Jet company notice that there is a market. But, to be accepted, the sonic boom of supersonic business jet has to be reduced.

A lot of work is done on reducing the sonic boom by modifying aircraft shape. The main problem is that there is no conventional shape to reduce the boom. First of all, it has been demonstrated that significant reduction in the shock overpressure levels is achieved by reducing the size, *i.e.,* the weight, of the aircraft. Indeed, if the weight of a supersonic jet is reduced from $340\,000$ kg ($750\,000$ lbs) to around $68\,000$ kg ($150\,000$ lbs) then the shock overpressure can be reduced from 143 Pa (3 psf) to about 76 Pa (1.6 psf) [29]. Consequently, focussing on business jets would be the first step.

Several companies all around the world are working to propose low boom shape supersonic jet. We can cite Lockheed Martin, Gulfstream Aerospace, Aerion, Boeing, Jaxa and Dassault Aviation. They are involved in several programs: Quiet Supersonic Platform (QSP) in US, HIgh Speed AirCraft (HISAC) in Europ and Silent Supersonic Technology Demonstration Program (S3TD) in Japan.

Shape optimization for supersonic jet considers aerodynamic coefficients and the sonic boom. It results in complicated problem as the reduction of the drag and the reduction of sonic boom are two contradictory objectives. Indeed, for supersonic speed, low drag shape are sharp implying a high level of boom as shock waves are attached. This purpose is illustrated by the large variety of shape proposed in all projects. Nevertheless, some basic idea have a major impact on the sonic boom. For instance, placing the engines over the wings causes the shielding of shocks, thus reducing the sonic boom loudness on the ground. A more challenging achievement is to delay the coalescing of the little shock waves into an N wave. Splitting the first shock into several ones enables to increase the rise time and thus reduces the annoyance in the human perception of the boom. But, from higher up, a shock wave has more time to be attenuated by the atmosphere on its way to the ground, but it can also coalesce into an N wave. And a higher-flying jet requires larger wings and a bigger engine. Another tradeoff is between an airplane speed and its engine size and other design parameters. As a consequence, optimum Mach number seems to be about 1.6 to 1.8. At those Mach numbers, the optimum cruise altitude is about $15\,240$ to $16\,764$ meters ($50\,000$ to $55\,000$ feet).

Two innovative shape have already been realized and tested in the US with sonic boom measurement in the mid-field and on the ground. They pointed out that it is possible to reduce the sonic boom. There are the Shaped Sonic Boom Demonstration (SSBD) which is a modified body of F5-E and the Gulfstream Quiet Spike that has been added on a F15B. The first one reduces the amplitude of the first shock by breaking it [26]. The second aims at breaking the first shock into several ones so as to increase the rise time and to modify the human perception of the boom [19].

In this paper, we will compare two shapes provided by Dassault Aviation during HISAC European project. The first one is a low drag shape and the second one is a low boom shape with integrated engine, see Figure 16.

3 CFD Modeling

The near-field flow around the aircraft is modeled by the conservative Euler equations. Assuming that the gas is perfect, inviscid and that there is no thermal diffusion, the Euler equations for mass, momentum and energy conservation read:

$$\left\{\begin{array}{rcl} \dfrac{\partial \rho}{\partial t} + \nabla.(\rho \mathbf{U}) & = & 0\,, \\ \dfrac{\partial (\rho \mathbf{U})}{\partial t} + \nabla.(\rho \mathbf{U} \otimes \mathbf{U}) + \nabla p & = & 0\,, \\ \dfrac{\partial (\rho E)}{\partial t} + \nabla.((\rho E + p)\mathbf{U}) & = & 0\,, \end{array}\right.$$

where ρ denotes the density, $\mathbf{U}$ the velocity vector, $E = T + \frac{\|\mathbf{U}\|^2}{2}$ the total energy and $p = (\gamma - 1)\rho T$ the pressure with $\gamma = 1.4$ the ratio of specific heats and T the temperature. These equations can be

rewritten:

$$\frac{\partial W}{\partial t} + \nabla \cdot F(W) = 0\,, \tag{1}$$

where $W = {}^t(\rho, \rho\mathbf{U}, \rho E)$ is the conservative variables vector and the matrix F represents the convective operator.

The Euler system is solved with a Finite Volume technique on unstructured tetrahedral meshes using `Wolf`, a in-house flow solver. The resolution is performed on highly anisotropic adapted meshes to enhance drastically the accuracy of the simulations. This is a (the only) way to propagate mach cone emitted by the aircraft several kilometers below in the mid-field. The flow solver and the mesh adaptation methods are presented in the following sections. A last section validates the approach on a test case proposed by NASA [5].

3.1 Flow solver

The proposed Finite Volume scheme is vertex-centered and uses a particular edge-based formulation with upwind elements. This flow solver employs the HLLC or the Roe approximate Riemann solver to compute numerical fluxes. High-order scheme is derived according to a MUSCL (Monotone Upwind Schemes for Conservation Laws) type method using downstream and upstream tetrahedra. This approach is compatible with vertex-centered and edge-based formulations. Consequently, an inexpensive high-order extension of monotone upwind schemes is easily derived. The flux integration based on the edges and their corresponding upwind elements (crossed by the edge) is a key-feature in order to preserve the positivity of the density for vertex-centered formulation. The MUSCL type method is combined with a generalization of the Superbee limiter with three entries to guarantee the TVD (Total Variation Diminishing) property of the scheme. An explicit time stepping algorithm is used by means of a strong-stability-preserving (SSP) Runge-Kutta scheme.

3.1.1 Scheme for convective fluxes

The considered method is a vertex-centred Finite Volume scheme applied to tetrahedral unstructured meshes which uses a particular edge-based formulation with upwind elements introduced in [9]. This formulation consists in associating to each vertex P_i of the mesh a control volume or finite-volume cell, denoted C_i. The dual finite-volume cell mesh is built by the rule of medians. The common boundary $\partial C_{ij} = \partial C_i \cap \partial C_j$ between two neighboring cells C_i and C_j is decomposed in several triangular interface facets. An illustration of this construction in two dimensions is shown in Figure 4.

Hence applying the Finite Volume method to the Euler equations, we get for each finite volume cell C_i:

$$|C_i|\frac{dW_i}{dt} + \int_{\partial C_i} F(W_i)\cdot \mathbf{n}_i \, d\gamma = 0\,, \tag{2}$$

where W_i is the mean value of the solution W on the cell C_i. The integration of the convective fluxes F is computed by decomposing the cell boundary in facets ∂C_{ij}:

$$\int_{\partial C_i} F(W_i^n) \cdot \mathbf{n}_i \, d\gamma \; = \sum_{P_j \in \mathcal{V}(P_i)} F|_{I_{ij}} \cdot \int_{\partial C_{ij}} \mathbf{n}_i \, d\gamma \, ,$$

where $\mathcal{V}(P_i)$ is the set of all neighboring vertices of P_i, $\mathbf{n}_i$ is the outer normal to the cell C_i and $F|_{I_{ij}}$ represents the constant value of $F(W)$ at the interface ∂C_{ij}.

The flow is calculated with a numerical flux function, denoted Φ_{ij}:

$$\Phi_{ij} = \Phi_{ij}(W_i, W_j, \mathbf{n}_{ij}) = F|_{I_{ij}} \cdot \int_{\partial C_{ij}} \mathbf{n}_i \, d\gamma \, , \tag{3}$$

where $\mathbf{n}_{ij} = \displaystyle\int_{\partial C_{ij}} \mathbf{n}_i \, d\gamma$. The numerical flux function approximates the hyperbolic terms on the common boundary ∂C_{ij}. We notice that the computation of the convective fluxes is performed mono-dimensionnaly in the direction normal to the boundary of the finite volume cell. Therefore, the numerical calculation of the flux function Φ_{ij} at the interface ∂C_{ij} is achieved by the resolution of a one-dimensional Riemann problem in the direction of the normal $\mathbf{n}_{ij}$ by means of an approximate Riemann solver.

Several upwind numerical flux functions are available and can be formally written:

$$\Phi_{ij}(W_i, W_j, \mathbf{n}_{ij}) = \frac{F(W_i) + F(W_j)}{2} \cdot \mathbf{n}_{ij} + d\left(W_i, W_j, \mathbf{n}_{ij}\right) \, , \tag{4}$$

where the function $d\left(W_i, W_j, \mathbf{n}_{ij}\right)$ contains the upwind terms and depends on the chosen scheme.

In this paper, we compare the Roe and the HLLC Riemann solver that we summarize below. More details on Roe solver and HLLC solver are found in [32] and [3], respectively.

Roe Riemann solver. In the Roe approach, the upwinding term d is defined by the Jacobian matrix of F:

$$A(W) = \frac{\partial (F(W) \cdot \mathbf{n}_{ij})}{\partial W} \, .$$

The eigenvalues of $A(W)$ are real and given by u, $u + c$ and $u - c$. In the context of the Euler equations, the hyperbolic flux is homogeneous of order one leading to the property:

$$F(W) \cdot \mathbf{n}_{ij} = A(W) \, W \, ,$$

that enables non-oscillatory conservative schemes to be built. The flux resolution uses the formulation of Φ introduced by Roe:

$$\Phi^{Roe}(W_i, W_j, \mathbf{n}_{ij}) = \frac{F(W_i) + F(W_j)}{2} \cdot \mathbf{n}_{ij} + |\tilde{A}(W_i, W_j)| \frac{W_i - W_j}{2} \, ,$$

where $\tilde{A}$ is the Jacobian of F evaluated for the Roe average variables and for a diagonalizable matrix $A = P\Lambda P^{-1}$ we have denoted $|A| = P|\Lambda|P^{-1}$. Let W_l and W_r be the two states, then the Roe averages are given by:

$$\tilde{\rho} = \sqrt{\rho_l \rho_r}\,, \quad \tilde{\mathbf{U}} = \frac{\sqrt{\rho_l}\,\mathbf{U}_l + \sqrt{\rho_r}\,\mathbf{U}_r}{\sqrt{\rho_l} + \sqrt{\rho_r}} \quad \text{and} \quad \tilde{H} = \frac{\sqrt{\rho_l} H_l + \sqrt{\rho_r} H_r}{\sqrt{\rho_l} + \sqrt{\rho_r}}$$

from which we get Roe average sound speed: $\tilde{c}^2 = (\gamma - 1)\,(\tilde{H} - \frac{1}{2}\tilde{q}^2)$ where $\tilde{q}^2 = \|\tilde{\mathbf{U}}\|^2$.

HLLC Riemann solver. The idea of the HLLC flow solver is to consider locally a simplified Riemann problem with two intermediate states depending on the local left and right states. The simplified solution to the Riemann problem consists of a contact wave with a velocity S_M and of two acoustic waves, which may be either shocks or expansion fans. The acoustic waves have the smallest and the largest velocities (S_L and S_R, respectively) of all the waves present in the exact solution. If $S_L > 0$ then the flow is supersonic from left to right and the upwind flux is simply defined from $F(W_l)$ where W_l is the state on the left of the discontinuity. Similarly, if $S_R < 0$ then the flow is supersonic from right to left and the flux is determined by $F(W_r)$ where W_r is the state on the right of the discontinuity. In the more difficult subsonic case when $S_L < 0 < S_R$ we have to calculate $F(W_l^*)$ or $F(W_r^*)$. Consequently, the HLLC flux is given by:

$$\Phi^{HLLC} = \begin{cases} F_l & \text{if } S_L > 0 \\ F_l^* & \text{if } S_L \leq 0 < S_M \\ F_r^* & \text{if } S_M \leq 0 \leq S_R \\ F_r & \text{if } S_R < 0 \end{cases}$$

Now, let us specify how W_l^* and W_r^* are evaluated. We denote by $\eta = \mathbf{U}.\mathbf{n}$. In [3], the following evaluation is proposed:

$$\begin{aligned} F_l^* &= F_l + S_L(W_l^* - W_l) \\ F_r^* &= F_r + S_R(W_r^* - W_r)\,. \end{aligned}$$

from which the W_l^* and W_r^* are computed. Assuming that $\eta^* = \eta_l^* = \eta_r^* = S_M$, we obtain (the subscript $_l$ or $_r$ are omitted for clarity)

$$W^* = \frac{1}{S - S_M} \begin{pmatrix} \rho\,(S-\eta) \\ \rho\mathbf{U}\,(S-\eta) + (p^* - p)\mathbf{n} \\ \rho E\,(S-\eta) + p^* S_M - p\eta \end{pmatrix} = \frac{1}{S - \eta^*} \begin{pmatrix} \rho\,(S-\eta) \\ \rho\mathbf{U}\,(S-\eta) + (p^* - p)\mathbf{n} \\ \rho E\,(S-\eta) + p^* \eta^* - p\eta \end{pmatrix}$$

where

$$p^* = \rho\,(S-\eta)(S_M - \eta) + p\,.$$

The key of this solver lies in the definition of the three waves velocity. For the contact wave, the following velocity is considered:

$$S_M = \frac{\rho_r \eta_r (S_R - \eta_r) - \rho_l \eta_l (S_L - \eta_l) + p_l - p_r}{\rho_r (S_R - \eta_r) - \rho_l (S_L - \eta_l)}\,,$$

and the other acoustic wave speeds are based on the Roe averages:

$$S_L = \min(\eta_l - c_l, \tilde{\eta} - \tilde{c}) \quad \text{and} \quad S_R = \max(\eta_r + c_r, \tilde{\eta} + \tilde{c})\,.$$

With such waves velocities, the HLLC Riemlann solver has the following properties. It automatically: (i) satisfies the entropy inequality, (ii) resolves isolated contacts exactly, (iii) resolves isolated shocks exactly and (iv) preserves positivity.

Such a formulation gives at best only a first-order scheme. However, higher-order extensions are possible with a MUSCL type technique.

3.1.2 High-order accurate version

The MUSCL type reconstruction method has been designed to increase the order of accuracy of the scheme. This method was introduced by Van Leer in a series of papers, see for instance [22]. The idea is to use extrapolated values W_{ij} and W_{ji} of W at the interface ∂C_{ij} to evaluate the flux, cf. Figure 4. The following approximation is performed:

$$\Phi_{ij} = \Phi_{ij}(W_{ij}, W_{ji}, \mathbf{n}_{ij})\,,$$

with W_{ij} and W_{ji} which are linearly interpolated as:

$$\left\{ \begin{array}{rcl} W_{ij} & = & W_i + \dfrac{1}{2}\,(\nabla W)_{ij} \cdot \overrightarrow{P_i P_j}\,, \\ W_{ji} & = & W_j + \dfrac{1}{2}\,(\nabla W)_{ji} \cdot \overrightarrow{P_j P_i}\,. \end{array} \right. \tag{5}$$

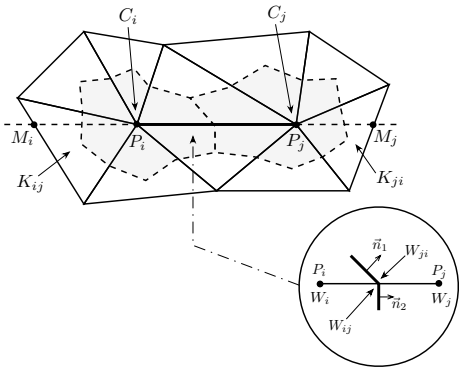

Figure 4: *Illustration of finite volume cells construction in two dimensions with two neighboring cells C_i and C_j, and the upwind triangles K_{ij} and K_{ji} associated to the edge P_iP_j. Definition of the common boundary ∂C_{ij} with the representation of the solution extrapolated values for the MUSCL type approach.*

where, in contrast to the original MUSCL approach, the approximate "slopes" $(\nabla W)_{ij}$ and $(\nabla W)_{ji}$ are defined for any edge and obtained using a combination of centered, upwind and nodal gradients.

The centered gradient, which is related to the edge P_iP_j, is defined as:

$$(\nabla W)^C_{ij} \cdot \overrightarrow{P_iP_j} = W_j - W_i \, .$$

Upwind and downwind gradients, which are also related to edge P_iP_j, are computed according to the definition of upstream and downstream tetrahedra of the edge P_iP_j. These tetrahedra are respectively denoted K_{ij} and K_{ji}, cf. Figure 5. K_{ij} (resp. K_{ji}) is the unique tetrahedron of the ball of P_i (resp. P_j) the opposite face of which is crossed by the line defined by the edge P_iP_j. Upwind and downwind gradients are then defined for vertices P_i and P_j as:

$$(\nabla W)^U_{ij} = (\nabla W)|_{K_{ij}} \quad \text{and} \quad (\nabla W)^D_{ji} = (\nabla W)|_{K_{ji}} \, .$$

where $(\nabla W)|_K = \sum_{P \in K} W_P \nabla \phi_P|_K$ is the P_1-Galerkin gradient on tetrahedron K. Parametrized nodal gradients are built by introducing the β-scheme:

$$\begin{aligned} (\nabla W)_{ij} &= (1-\beta)(\nabla W)^C_{ij} + \beta\,(\nabla W)^U_{ij} \\ (\nabla W)_{ji} &= (1-\beta)(\nabla W)^C_{ij} + \beta\,(\nabla W)^D_{ij} \, , \end{aligned}$$

where $\beta \in [0,1]$ is a parameter controlling the amount of upwinding. For instance, the scheme is centered for $\beta = 0$ and fully upwind for $\beta = 1$.

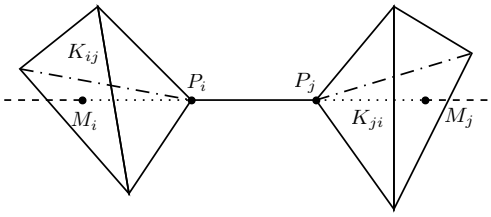

Figure 5: *Downstream K_{ij} and upstream K_{ji} tetrahedra associated to the edge $[P_i, P_j]$.*

Numerical dissipation of fourth-order: V4-scheme. The most accurate β-scheme is obtained for $\beta = 1/3$. Indeed, it can be demonstrated that this scheme is third-order for the two-dimensional linear advection on structured triangular meshes of Friedrichs-Keller type. In our case, for the non-linear Euler equations on unstructured meshes, a second-order scheme with a fourth-order numerical dissipation is obtained. This high-order gradient is given by:

$$\begin{aligned} (\nabla W)^{V4}_{ij} &= \frac{2}{3}\,(\nabla W)^C_{ij} + \frac{1}{3}\,(\nabla W)^U_{ij} \\ (\nabla W)^{V4}_{ji} &= \frac{2}{3}\,(\nabla W)^C_{ji} + \frac{1}{3}\,(\nabla W)^D_{ij} \, . \end{aligned}$$

Numerical dissipation of sixth-order: V6-scheme. An even less dissipative scheme has been proposed in [9]. It is a more complex linear combination of gradients using centered, upwind and nodal P_1-Galerkin gradients. The nodal P_1-Galerkin gradient of P_i is related to the cell C_i and is computed by averaging the gradients of all the tetrahedra containing the vertex P_i:

$$(\nabla W)_{P_i} = \frac{1}{4\,|C_i|} \sum_{K \in C_i} |K| (\nabla W)|_K \,.$$

A sixth-order dissipation scheme is then obtained by considering the following high-order gradient:

$$(\nabla W)_{ij}^{V6} = (\nabla W)_{ij}^{V4} - \frac{1}{30}\left((\nabla W)_{ij}^{U} - 2\,(\nabla W)_{ij}^{C} + (\nabla W)_{ij}^{D}\right) - \frac{2}{15}\left((\nabla W)_{M_i} - 2\,(\nabla W)_{P_i} + (\nabla W)_{P_j}\right)$$

$$(\nabla W)_{ji}^{V6} = (\nabla W)_{ji}^{V4} - \frac{1}{30}\left((\nabla W)_{ij}^{D} - 2\,(\nabla W)_{ij}^{C} + (\nabla W)_{ij}^{U}\right) - \frac{2}{15}\left((\nabla W)_{M_j} - 2\,(\nabla W)_{P_j} + (\nabla W)_{P_i}\right) \,,$$

where $(\nabla W)_{M_{i,j}}$ is the gradient at the points $M_{i,j}$ intersection of the line defined by P_iP_j and upwind/downwind tetrahedra. These gradients are computed by linear interpolation of the vertices attached nodal gradients of face containing $M_{i,j}$.

Dervieux limiter. The previous MUSCL schemes are not monotone. Therefore, limiting functions must be coupled with the previous high-order gradient evaluations to guarantee the TVD property of the scheme. The gradient of Relation (5) is substituted by a limited gradient denoted $(\nabla W)_{ij}^{lim}$. Here, we consider the three-entries limiter introduced by Dervieux which is a generalization of the Superbee limiter [8]:

$$\begin{array}{l} \text{if } uv \leq 0 \text{ then} \\ \quad Lim(u,v,w) = 0 \\ \text{else} \\ \quad Lim(u,v,w) = Sign(u)\, min(2\,|u|, 2\,|v|, |w|)\,, \end{array}$$

and we use: $Lim((\nabla W)_{ij}^{C}, (\nabla W)_{ij}^{D}, (\nabla W)_{ij}^{HO})$ where $(\nabla W)_{ij}^{HO}$ is even $(\nabla W)_{ij}^{V4}$ or $(\nabla W)_{ij}^{V6}$.

3.1.3 Boundary conditions

For aircraft supersonic flow simulations, three boundary conditions are required. Slip boundary conditions are imposed for the body as the flow is considered inviscid. We used Steger-Warming flux [35] to set up free-stream (external flow) conditions. And finally, for geometry with engines, the inlet and the exhaust are modeled with a modified Steger-Warming flux.

Slip condition. For this boundary condition we impose weakly

$$\mathbf{U}.\mathbf{n} = 0\,. \tag{6}$$

To this end, we compute the flux Φ between the state on the boundary W and a mirror state $\overline{W}$:

$$W = \begin{pmatrix} \rho \\ \rho\mathbf{U} \\ \rho E \end{pmatrix} \quad \text{and} \quad \overline{W} = \begin{pmatrix} \rho \\ \rho\mathbf{U} - 2\,\rho\,(\mathbf{U}.\mathbf{n})\,\mathbf{n} \\ \rho E \end{pmatrix}$$

If Condition (6) is verified then $W = \overline{W}$ and thus $\Phi(W, \overline{W}) = F(W)$. Moreover, as W verifies Relation (6), $F(W)$ simplifies to:

$$\Phi_{Slip} = F(W) = (0, p\,\mathbf{n}, 0)^t\,.$$

Therefore, if the desired condition is satisfied, then the boundary flux reduced to its well known commonly used form.

Nevertheless, the state W on the boundary doesn't satisfy this condition unless it is imposed strongly which is not possible as we will no more conserve the mass. Moreover, the direct use of this formulation can lead to negative density or pressure due to its inconsistency. This problem is solved by computing the flux between the state and its mirror state. This flux depends on the considered flux. Let us presents the Roe and the HLLC versions.

Roe flux. By definition, we have $c = \overline{c}$, $p = \overline{p}$ and $H = \overline{H}$. Notably, we get $\mathbf{U}.\mathbf{n} = -\overline{\mathbf{U}}.\mathbf{n}$. In this particular case, the Roe average simplify to

$$\tilde{\rho} = \rho\,, \quad \tilde{\mathbf{U}} = \mathbf{U} - (\mathbf{U}.\mathbf{n})\,\mathbf{n} = \mathbf{U_t} \quad \text{and} \quad \tilde{H} = H\,,$$

where $\mathbf{U_t}$ is the velocity in the tangent plane. We deduce:

$$\tilde{\mathbf{U}}.\mathbf{n} = 0\,, \quad \tilde{q}^2 = \|\mathbf{U_t}\|^2 = q^2 - (\mathbf{U}.\mathbf{n})^2 \quad \text{and} \quad \tilde{c}^2 = (\gamma - 1)\,(H - \frac{1}{2}\tilde{q}^2)\,,$$

Notice that the Roe average state verifies the slipping condition: $\tilde{\mathbf{U}}.\mathbf{n} = 0$. Computing analytically the Roe flux leads to :

$$\Phi_{Slip} = \Phi^{Roe}(W, \overline{W}, \mathbf{n}) = \Big(0, \big(p + \rho\,\tilde{c}\,(\mathbf{U}.\mathbf{n}) + \rho\,(\mathbf{U}.\mathbf{n})^2\big)\ \mathbf{n},\ 0\Big)^t\,.$$

This flux can be written shortly: $\Phi^{Roe}(W, \overline{W}, \mathbf{n}) = (0,\ p^\star\,\mathbf{n},\ 0)^t$.

HLLC flux. To compute Φ^{HLLC} we still have to evaluate Roe average to define waves speed. The left and right waves speed are then given by

$$S_L = \min(\mathbf{U}.\mathbf{n} - c, -\tilde{c}) \quad \text{and} \quad S_R = \max(-\mathbf{U}.\mathbf{n} + c, \tilde{c})\,.$$

Therefore, we always have $S_L < 0$ and $S_R > 0$, as $\tilde{c} > 0$. The flux is then given by one of the intermediate state W^*. But in this case, it simplifies again:

$$S^* = 0 = \mathbf{U}^*.\mathbf{n}$$

as $S_L + S_R = 0$ meaning that the intermediate state verifies the slipping condition. Finally, we get:

$$\Phi_{Slip} = \Phi^{HLLC}(W, \overline{W}, \mathbf{n}) = F(W^*) = (0,\ p^*\mathbf{n},\ 0)^t$$

with $p^* = p + \rho\,\mathbf{U}.\mathbf{n}\,(\mathbf{U}.\mathbf{n} - S_L) = p + \rho\,\mathbf{U}.\mathbf{n}\ \min(c, \tilde{c} + \mathbf{U}.\mathbf{n})$

Let us give two remarks about the proposed slip condition. If the Roe average wave speed is considered in the HLLC flux then we have $p^* = p^\star$ and thus $\Phi^{HLLC} = \Phi^{Roe}$ which is consistent. Moreover, if Condition (6) is verified, we get $p = p^\star = p^*$ and the computed flux become the usual one. The added term to the pressure acts as a correction term to take into account the violation of Condition (6) by the current state.

Free-stream condition. This condition imposes a free-stream uniform flow from the infinite. It applies when we have a boundary Γ_∞ for which the infinite constant state W_∞ is known. We assume that the infinite state is uniform:

$$W_\infty = \begin{pmatrix} \rho_\infty \\ (\rho \mathbf{U})_\infty \\ (\rho E)_\infty \end{pmatrix} .$$

This state enables upwind fluxes at the infinite to be computed. The considered boundary fluxes are built from a decomposition following the characteristics values. We consider the Steger-Warming flux [35] which is completely upwind on the solution W_i:

$$\Phi_\infty = A^+(W_i, \mathbf{n_i}) W_i + A^-(W_i, \mathbf{n_i}) W_\infty ,$$

where $A^+ = \dfrac{|A| + A}{2}$ and $A^- = \dfrac{|A| - A}{2}$.

Engine condition. Engines boundary conditions are defined by a given number of variables representing the engine data. All variables are linked by the isentropic relations that in particular connects the static state to the total state. These data are used to define the jet state W_{jet}. To set up the engine data, the flow solver requires:

- 3 data for the inlet : M^{in}, p_s^{in} and T_t^{in}
- 3 data for the exhaust : M^{out}, p_t^{out} and T_t^{out}

where subscript $_s$ and $_t$ denote the static and the total variables, respectively. Moreover, the direction of the flow is considered normal to the inlet or exhaust face: $\mathbf{U} = \|\mathbf{U}\|\mathbf{n}$. The flux is computed using a modified Steger and Warming boundary condition for inlet and exhaust:

$$\Phi_{jet} = A^+(W_{jet}, \mathbf{n_i})\, W_i + A^-(W_{jet}, \mathbf{n_i})\, W_{jet} ,$$

where W_{jet} and W_i are the engine constant state and the local vertex state, respectively.

3.1.4 Time advancing

An explicit scheme is used to advance the Euler equations in time by a line method, *i.e.,* time and space are treated separately. Once the equations have been discretized in space, a set of ordinary differential equations in time is obtained: $W_t - L(W) = 0$. To discretize the previous relation, a high-order multi-step Runge-Kutta scheme is considered. Such time discretization methods, called SSP (Strong-Stability-Preserving), have non-linear stability properties which are particularly suitable for the integration of system of hyperbolic conservation laws where discontinuities appear. These schemes verify the TVD property.

The optimal 2-stage order-2 SSP Runge-Kutta scheme introduced by Shu and Osher [33] is the following modified Euler scheme:

$$\begin{aligned} W^{(1)} &= W^n + \Delta t\, L(W^n) , \\ W^{n+1} &= \frac{1}{2} W^n + \frac{1}{2} W^{(1)} + \frac{1}{2} \Delta t\, L(W^{(1)}) , \end{aligned}$$

which accept to use a CFL coefficient up to 1. In this study, we consider a 5-stage order-2 SSPRK scheme with given in [34] that enables us to consider CFL coefficient up to 4. This scheme reads:

$$\begin{aligned} W^{(1)} &= W^n + \frac{1}{4}\Delta t\, L(W^n)\,, \\ W^{(k)} &= W^{(k-1)} + \frac{1}{4}\Delta t\, L(W^{(k-1)}),\ k = 2\dots 4\,, \\ W^{n+1} &= \frac{1}{5}W^n + \frac{4}{5}W^{(4)} + \frac{1}{5}\Delta t\, L(W^{(4)})\,, \end{aligned}$$

Computing the time step. The maximal allowable time step for the numerical scheme obtained on the linearized model is:

$$\Delta t(P_i) = \frac{h(P_i)}{c_i + \|\mathbf{U}_i\|}$$

where $h(P_i)$ is the smallest altitude in the ball of vertex P_i. The global time step is then given by $\Delta t = CFL \min_{P_i}(\Delta t(P_i))$. However, in the context of steady simulation, local time step are used to obtain considerable gain in CPU time. Each vertex advances in time at its own speed defined by the CFL condition.

3.2 Multi-scales anisotropic mesh adaptation

Mesh adaptation provides a way to control the accuracy of the numerical solution by modifying the domain discretization according to size and directional constraints. When dealing with real life flow problems, Hessian based unstructured mesh adaptation has already proved its efficiency to improve the ratio between the solution accuracy and the number of degrees of freedom (the problem complexity) [6, 12, 16, 23, 28, 36]. In addition, as a large number of physical phenomena are anisotropic by nature, anisotropic mesh adaptation improves even more this ratio. In the context of flow with shocks, anisotropic mesh adaptation provides very accurate solutions by reducing considerably the numerical dissipation of shock capturing schemes.

If previous features of unstructured mesh adaptation are quite classical, it has been recently pointed out that mesh adaptation has further consequences impacting directly numerical schemes used to approximate the flow. Indeed, a loss of convergence order generally occurs due to the presence of steep gradients (Naviers Stokes equations) or genuine discontinuities (Euler equations) in the flow, even if a probably spatially high order method is employed. The computed mesh convergence order on uniformly refined meshes is not the theoretical expected one. In [25], it has been demonstrated that the convergence order of numerical schemes can be recovered thanks to this mesh adaptation procedure. Next sections summarize the considered anisotropic mesh adaptation method.

3.2.1 Anisotropic mesh generation

The generation of anisotropic adapted meshes uses the notion of length in a metric space [13]. The idea is to introduce a metric tensor in the dot product definition to modify size evaluation in all

directions. A metric is a $n \times n$ symmetric definite positive matrix, where n is the space dimension. The mesh is automatically adapted by generating *a unit mesh* with respect to this metric, *i.e.,* the mesh is such that all edges have a length close to one in the metric and such that all elements are almost regular. The mesh is then uniform in prescribed metric space and, non-uniform and anisotropic in the Euclidean space.

In the context of numerical simulation, the accuracy level of the solution depends on the current mesh used for its computation and the mesh adaptation prescription, *i.e.,* the metric field, is provided by the current solution. This points out the non-lineraity of the anisotropic mesh adaptation problem. Therefore, an iterative process needs to be set up in order to converge both the mesh and the solution, or equivalently the metric field and the solution.

Mesh adaptation scheme. For stationary simulations, an adaptive computation is carried out *via* a mesh adaptation loop inside which an algorithmic convergence of the couple mesh-solution is sought. In other words, the goal is to converge towards the stationary solution of the problem and similarly towards the corresponding invariant adapted mesh. At each stage, a numerical solution is computed on the current mesh with the flow solver. This solution is analyzed with an error estimate presented in the following section. This error estimate is based on the control of the interpolation error in $\mathbf{L}^p$ norm and exhibit a metric field. This anisotropic metric is a function of the Hessian of the solution which is reconstructed from the numerical solution. Next, an adapted mesh, *i.e.,* a unit mesh, is generated with respect to this metric. Mesh generators use all the meshing operations to adapt the mesh and a vertex insertion procedure based on an anisotropic generalization of Delaunay technique [11, 15]. Finally, the solution is linearly interpolated on the new mesh. This procedure is repeated until convergence of the couple mesh-solution is reached.

3.2.2 Continuous mesh model and optimality

Let u be an analytic solution defined on a bounded domain Ω and let N_{ver} be the desired number of vertices for the mesh. We aim at creating the optimal mesh $\mathcal{H}$ that minimizes the interpolation error $(u - \Pi_h u)$ in $\mathbf{L}^p$ norm with N vertices. $\Pi_h u$ denotes the linear interpolate of u on $\mathcal{H}_{ver}$. This problem is ill-posed. The idea is to formulate it in a continuous framework.

A continuous model of a mesh provided by a riemannian metric space, or a metric in short, has been proposed in [2, 10, 24, 25]. In the following, we specify how the continuous mesh or metric $\mathcal{M}$ is derived. First, a continuous analog of the linear interpolation error is defined for this metric: $u - \pi_{\mathcal{M}} u$ where $\pi_{\mathcal{M}} u$ is the continuous linear interpolate. Then, we solve analytically the well-posed problem:

$$\text{Find } \mathcal{M}_{opt} \text{ of complexity } \mathcal{C}(\mathcal{M}_{opt}) = N \text{ such that } \mathcal{E}_{\mathcal{M}_{opt}}(u) = \min_{\mathcal{M}} \|u - \pi_{\mathcal{M}} u\|_{\mathcal{M}, \mathbf{L}^p(\Omega)}\,, \quad (7)$$

where the metric complexity is given by

$$\mathcal{C}(\mathcal{M}) = \int_\Omega \sqrt{\det(\mathcal{M}(\mathbf{x}))}\, \mathrm{d}\mathbf{x} = \int_\Omega \frac{1}{\Pi_i h_i(\mathbf{x})}\, \mathrm{d}\mathbf{x} = N,$$

and h_i are the sizes prescribed by the metric for its principal directions.

The point-wise continuous interpolation error $e_{\mathcal{M}}(\mathbf{x}) = |u(\mathbf{x}) - \pi_{\mathcal{M}} u(\mathbf{x})|$ has been derived in [2, 24]. We proved that locally the optimal metric has for main directions the eigenvectors of the Hessian of u. Let $\mathcal{R}_u$ and Λ be the Hessian eigenvectors and eigenvalues matrices. Then, the point-wise error model for a point $\mathbf{a}$ simplifies to:

$$e_{\mathcal{M}}(\mathbf{a}) = \sum_{i=1}^{n} h_i^2(\mathbf{a}) \left| \frac{\partial^2 u}{\partial {\alpha_i}^2}(\mathbf{a}) \right|,$$

where $\dfrac{\partial^2 u}{\partial {\alpha_i}^2}$ stands for the eigenvalues of the Hessian in the direction of the i^{th} eigenvectors of the Hessian. Optimization problem (7) is then solved analytically by a calculus of variation. The resulting optimal n-dimensional metric reads:

$$\mathcal{M}_{\mathbf{L}^p} = D_{\mathbf{L}^p} \left(\det |H_u|\right)^{\frac{-1}{2p+n}} \mathcal{R}_u \left|\Lambda\right| {}^t\mathcal{R}_u \quad \text{with} \quad D_{\mathbf{L}^p} = N^{\frac{2}{n}} \left(\int_\Omega \left(\det |H_u|\right)^{\frac{p}{2p+n}} \right)^{-\frac{2}{n}}. \tag{8}$$

$D_{\mathbf{L}^p}$ is a global normalization term set to obtain a continuous mesh with a complexity N and $\left(\det |H_u|\right)^{\frac{-1}{2p+n}}$ is a local normalization term accounting for the sensitivity of the $\mathbf{L}^p$ norm. Indeed, the choice of a $\mathbf{L}^p$ norm is essential in a mesh adaptation process regarding the type of problems solved. For instance in CFD, physical phenomena can involve large scale variations. Capturing weak phenomena is crucial for obtaining an accurate solution by taking into account all phenomena interactions in the main flow area. Intrinsically, metrics constructed with lower p norms are more sensitive to weaker variations of the solution whereas the $\mathbf{L}^\infty$ norm mainly concentrates on strong singularities (e.g. shocks).

This continuous mesh model represents a class of equivalence of meshes. More precisely, a metric is seen as a continuous representative of the class of all meshes having the same global interpolation error level value for a given number of vertices. An "optimal" mesh $\mathcal{H}$ minimizing $\|u - \Pi_h u\|_{\mathbf{L}^p(\Omega_h)}$ is thus obtained by projecting the optimal continuous mesh $\mathcal{M}_{\mathbf{L}^p}$ into the space of discrete meshes by means of an adaptive mesh generator. The projection is realized by generating a unit mesh for the metric $\mathcal{M}_{\mathbf{L}^p}$, *i.e.,* all edges have a length close to one and all the elements are regular.

Mesh convergence order. The expression of the error committed with the optimal metric $\mathcal{M}_{\mathbf{L}^p}$ is:

$$\mathcal{E}(\mathcal{M}_{\mathbf{L}^p}) = nN^{-\frac{2}{n}} \left(\int_\Omega \left(\det |H_u|\right)^{\frac{p}{2p+n}} \right)^{\frac{2p+n}{pn}} \leq \frac{Cst}{N^{2/n}}. \tag{9}$$

Two major results arise from this relation:

- the interpolation error obtained with the resulting metric $\mathcal{E}(\mathcal{M}_{\mathbf{L}^p})$ is optimal in $\mathbf{L}^p$ norm, *i.e.,* a larger error is committed whatever the considered continuous mesh of complexity N (see [2] for the proof)

- a global second-order asymptotic mesh convergence is expected for the considered variable u even if singularities are present in the flow field for all p.

As regards the mesh convergence order, a simple analogy with regular grids leads to consider that $N = O\left((\Pi_{i=1,n} h_i)^{-1}\right) = O\left((h^n)^{-1}\right)$ so that the previous estimate becomes: $\mathcal{E}(\mathcal{M}_{\mathbf{L}^p}) \leq Cst' h^2$.

3.2.3 Application to numerical computation

In our case, the numerical solution provides a continuous piecewise linear by elements representation of the solution. Consequently, our analysis cannot be applied directly to the numerical solution. The idea is to build a higher order solution approximation u^* of u from u_h which is twice continuously differentiable and to consider u^* in our error estimate. More precisely, the interpolation error is approximated as $\|u - \Pi_h u\|_\Omega \approx \|u^* - \Pi_h u^*\|_\Omega$. If u^* and u_h coincide at mesh vertices then we have $\|u^* - \Pi_h u^*\|_\Omega = \|u^* - u_h\|_\Omega$ illustrating that our estimate approximate the approximation error. Practically, only the Hessian of u^* is recovered. Two recovery or reconstruction of the Hessian of u^* from u_h, that are compared in this paper, are presented below.

In the context of discontinuous flows, the numerical solution is also piecewise linear by elements even if it approximates a discontinuous solution. The mesh acts as a regularization operator on the solution. In this case, we still approximate the solution u with a continuous higher order representation and we still apply our error estimate. Notice that, even if the numerical solution approximates discontinuous fields, it is continuous due to the numerical dissipation of the numerical scheme.

Let us introduce some notations used in the Hessian recovery methods. Let $\mathcal{T}_h$ be a mesh of a domain $\Omega \subset \mathbb{R}^d$. We denote by $\varphi_i \in V_h$ the basis function associated to vertex P_i, where V_h is the approximation space associated to the P^1 Lagrange finite element. We denote by S_i the stencil φ_i, *i.e.,* $S_i = supp\, \varphi_i$, which is in fact the ball of P_i.

A double $\mathbf{L}^2$-projection. The local $\mathbf{L}^2$-projection operator is based on the Clément interpolation operator [7]. The idea is to find, in a L^2-norm sense, the best constant gradient on S_i approximating the piecewise constant field ∇u_h. For each vertex P_i, we obtain the following gradient reconstruction:

$$\nabla_R u_h(P_i) = \frac{\sum_{K \in S_i} |K| \nabla(u_{h|K})}{|S_i|},$$

where $|K|$ and $|S_i|$ denote the volume of the element K and the stencil S_i, respectively. In fact, this procedure is equivalent to a reconstruction by means of a volume-weighted averaging.

The recovery procedure provides us with gradient nodal values and thus we get a piecewise linear by elements representation of the gradient. Consequently, the same recovery procedure can be applied to each component of the gradient to recover the Hessian of u^*.

A Green formulation. The Hessian of the solution is recovered using a weak formulation, based on the Green formula, considering that the gradient of u_h is constant by element. We consider the

same notations as previously. For each vertex P_k of $\mathcal{T}_h$, we have for $1 \leq i,j \leq d$:

$$\begin{aligned}\int_{\mathcal{T}_h} \frac{\partial^2 u_h}{\partial x_i \partial x_j}\,\varphi_k &= \int_{S_k} \frac{\partial^2 u_h}{\partial x_i \partial x_j}\,\varphi_k\,,\\ &= -\int_{S_k} \frac{\partial u_h}{\partial x_j}\,\frac{\partial \varphi_k}{\partial x_i} + \int_{\partial S_k} \frac{\partial u_h}{\partial n}\,\varphi_k\,d\sigma\,,\\ &= -\sum_{K\in S_k} \int_K \frac{\partial u_h}{\partial x_j}\,\frac{\partial \varphi_k}{\partial x_i}\,,\end{aligned}$$

as the shape function is zero on the boundary of the stencil ∂S_k. Specific treatment are done close to the boundary. Each component of the Hessian is then recovered with the relation:

$$\frac{\partial^2 u^*}{\partial x_i \partial x_j}(P_k) := \frac{-\displaystyle\int_{S_k} \frac{\partial u_h}{\partial x_j}\,\frac{\partial \varphi_k}{\partial x_i}}{\displaystyle\int_{S_k} \varphi_k} = -\frac{\displaystyle\sum_{K\in S_k} (\frac{\partial u_h}{\partial x_j})_{|K} \int_K \frac{\partial \varphi_k}{\partial x_i}}{\dfrac{|S_k|}{d+1}}\,,$$

with is equivalent to lump the mass matrix of the left-hand-side of the previous relation.

Remark 3.1. *The main difference between these two Hessian recovery procedures is the size of the stencil. A stencil of order* 2 *is used for the double* $\mathbf{L}^2$*-projection, whereas a stencil of order* 1 *is employed for the Green formulation. Consequently, reconstructed Hessian are sharper with the Green formulation. On the other hand, the* $\mathbf{L}^2$*-projection introduces an implicit smoothing.*

3.3 CFD validation by comparison to experimental data

The flow solver `Wolf` coupled with the multi-scales anisotropic mesh adaptation method is validated by comparing on an analytical geometry the numerical results, *i.e.,* mid-field pressure signatures, to experimental data obtained in a wind-tunnel by NASA in an experimental study [5]. As in Reference [21], Model 8 of Ref. [5] was selected to validate the proposed approach. This model represents two tandem cones connected by a cylinder defined analytically in inches by:

$$\begin{aligned} r &= x\sqrt{\frac{0.08}{\pi}} && \text{if} \quad 0 \leq x \leq 0.25\,l\\ r &= \sqrt{\frac{0.02}{\pi}} && \text{if} \quad 0.25\,l \leq x \leq 0.75\,l\\ r &= \frac{2}{2+\sqrt{2}}\sqrt{\frac{0.04}{\pi}}\left(x - \frac{2-\sqrt{2}}{2}\right) && \text{if} \quad 0.75\,l \leq x \leq l\,, \end{aligned}$$

with a reference length $l = 2$ inches (5.08 centimeters). The initial geometry has been elongated by adding a cylinder of length $2\,l$ to represent the sting support of the wind-tunnel. This geometry is illustrated in Figure 6. The geometry is immersed in a cylindrical domain aligned with the x-axis.

The cylinder has a length of 6 meters (236 inches) and a radius of 2.5 meters (98 inches). The computation is deliberately fully three-dimensionnal and do not use any axisymmetric reduction to reduce computational cost. Indeed, the aim is to validate the 3D platform which will be used for complete aircrafts configurations that are obviously not axisymmetric. The flow conditions are Mach 1.41 at 0° angle of attack.

While validating the adaptive simulation platform on this test case, the following parameters of the platform are compared:

- HLLC and Roe approximate Riemann solver
- V4-scheme and V6-scheme
- $\mathbf{L}^2$-projection and Green Hessian recovery method.

All ran cases are summarized in Table 1.

Case	Solver	Scheme	Hessian	$\mathcal{T}_{end}$ # vertices	$\mathcal{T}_{end}$ # tetrahedra
1	HLLC	V4	$\mathbf{L}^2$-projection	5 107 296	30 315 882
2	Roe	V4	$\mathbf{L}^2$-projection	4 295 057	25 464 860
3	HLLC	V4	Green	4 306 398	25 539 731
4	HLLC	V6	$\mathbf{L}^2$-projection	5 496 361	32 615 241
5	HLLC	V6	Green	4 161 098	24 661 706

Table 1: *All simulations cases for double-cone spike geometry. For each case, the final adapted mesh size is given.*

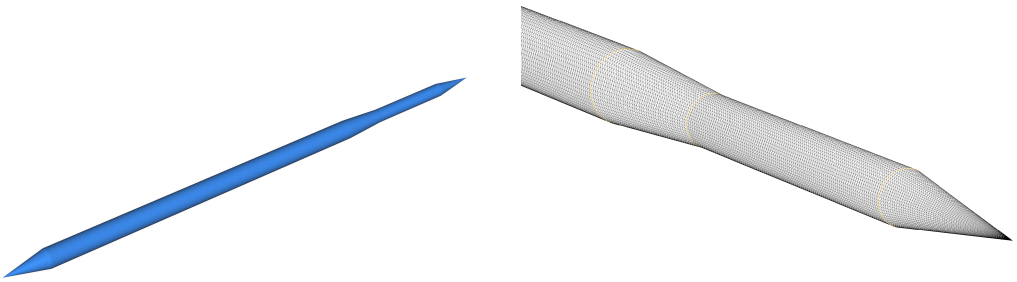

Figure 6: *Double-cone spike geometry and surface mesh.*

The initial uniform mesh is composed of $243\,446$ vertices and $1\,163\,402$ tetrahedra. As regards mesh adaptation, the Mach number is chosen as sensitive variable and its interpolation error is controlled $\mathbf{L}^2$ norm. A total of 15 adaptation iterations are performed. They are split into 3 steps of 5 adaptations with an increasing complexity:

$$[200\,000,\ 400\,000,\ 800\,000].$$

At each step, the couple mesh-solution is algorithmically converged at a fixed complexity. Considering an increasing dynamic complexity level has the advantage to accelerate the convergence of the whole process. In each case, we compared the final solution obtained on the final adapted mesh of almost 5 millions vertices and 30 millions tetrahedra. To illustrate the kind of mesh obtained, the final mesh obtained for the case 5 is shown in Figures 8 and 7.

Results are analyzed by extracting the mid-field pressure signatures along lines at various distances under the geometry from 5 to 20 body lengths. More precisely, we plot:

$$\Delta p = \left(\frac{R}{l}\right)^{\frac{3}{4}} \frac{p - p_\infty}{p_\infty} \text{ function of } \Delta x = \frac{x}{l}\left(\frac{R}{l}\right)^{-\frac{1}{4}},$$

where R the distance to the body. More details on notations and the extraction procedure are given in Section 4.2. Signatures are compared against NASA experimental wind-tunnel data given in Reference [5]. For all the cases, the agreement with experimental data is excellent. They are exemplified in Figures 9, 10 and 11. Notice that in [5], it is specified that the rounding of the measured pressure peaks is believed to be due in part to wind-tunnel vibration and boundary layer effects. Therefore, sharp shock wave peaks obtained in our simulations are the good answer. Lastly, always in [5], Whitham linear supersonic theory shown good agreement for very simple geometry but discrepancies for the current geometry appear. Whereas the present pressure signatures match the wind-tunnel data. This illustrate the benefits of the proposed approach which will be even more crucial when dealing with complex aircraft geometries. The discussion on Whitham theory will be pursued in Section 4.2.

To compare the numerical results, two points conduct our analysis on the mid-field signature:

1. the sharpness and the intensity of the shock waves at $R/l = 20$. In Section 4.2, we will see that the pressure decrease law in the mid-field is proportional to $(R/l)^{\frac{3}{4}}$ and the time length of the wave grows in $(R/l)^{\frac{1}{4}}$. And asymptotically, the pressure decrease law is in $(R/l)^{\frac{1}{2}}$. Therefore, the shocks amplitude must preserved (or increased) through the propagation, else it points out a numerical dissipation of the flow solver.

2. the last two shocks that are located between $\Delta x = 0.2$ and $\Delta x = 0.4$ at $R/l = 5$ are still separated at $R/l = 10$. This means that the two last shocks focalize at a distance between $R/l = 10$ and $R/l = 20$. If the two shocks have focalized before $R/l = 10$, it is an artifact due to the numerical dissipation of the flow solver.

In all cases, the Dervieux limiter is specified and the 5-stage order-2 SSPRK scheme is used for the time integration.

Roe vs. HLLC. The comparison between the Roe and the HLLC Riemann solvers is presented in Figure 9. For the analysis, both schemes are coupled with the V4-scheme and the $\mathbf{L}^2$-projection Hessian recovery which correspond to case 1 and 2. As expected, Roe is more accurate than HLLC. The difference in accuracy between each case is highlighted on the last two shocks that are not still merged at $R/l = 10$ for Roe. Moreover, the numerical dissipation of the solver is identified by the loss of intensity of the first shock peak which must remain constant. This phenomena is weaker with the Roe Riemann solver.

However, for robustness purposes, we prefer the HLLC Riemann solver as on more complex geometries with complex boundary conditions, such as real aircraft with engine presented in Section 5, Roe Riemann solver leads to negative pressures.

$\mathbf{L}^2$-projection vs. Green. The Hessian recovery methods are compared by using the HLLC Riemann solver and by considering either the V4-scheme (case 1 and 3) shown in Figure 10 or the V6-scheme (case 4 and 5) presented in Figure 11. The Green reconstruction is clearly the best choice than the $\mathbf{L}^2$-projection for this application. Indeed, in case 1 and 4 the separation between the two last shocks disappeared at $R/l = 10$ whereas this separation is still present in case 3 and 5 with the Green reconstruction in spite of the fact that adapted meshes with the Green reconstruction contain one million less vertices. This difference in accuracy is essentially due to the smallest (minimal) stencil of the Green recovery procedure. It results that the information to compute the metric is more compact (a three-vertices stencil) with the Green formulation than with the $\mathbf{L}^2$-projection reconstruction (a five-vertices stencil). Therefore, larger second derivatives are computed in the direction normal to shock waves implying smallest sizes to be prescribed by the metric along shock waves. Notice that in both cases,

V4-scheme vs. V6-scheme. The V6-scheme improves pressure signatures whatever the considered Riemann solver or the considered Hessian construction. This impact is highlighted when comparing Figures 10 and 11. Even if this scheme was initially designed to capture more accurately smooth solutions, such as vortices or instabilities, it also computes sharper shocks and reduce the numerical dissipation when propagating shocks.

Conclusion. The combination HLLC Riemann solver, V6-scheme and Green formulation for the Hessian recovery provides very accurate results agreeing with the experimental data, cf. Figure 11 right. The shock waves are not dissipated during the propagation and the shock sharpness is preserved. It demonstrates the ability of unstructured CFD flow solvers coupled with mesh adaptation to provide accurate results in the mid-field, here $R/l = 20$.

3.4 CFD validation without experimentation

When no experimental data are available, the computations can be validated by checking the convergence order of the method. In our case, the second order predicted by the theory has to be asymptotically attained on a series of (almost) embedded meshes. This will be done in Section 5 to validate the aircraft simulations. Another possible approach is to match in the mid-field the CFD pressure signal with a signal propagated.

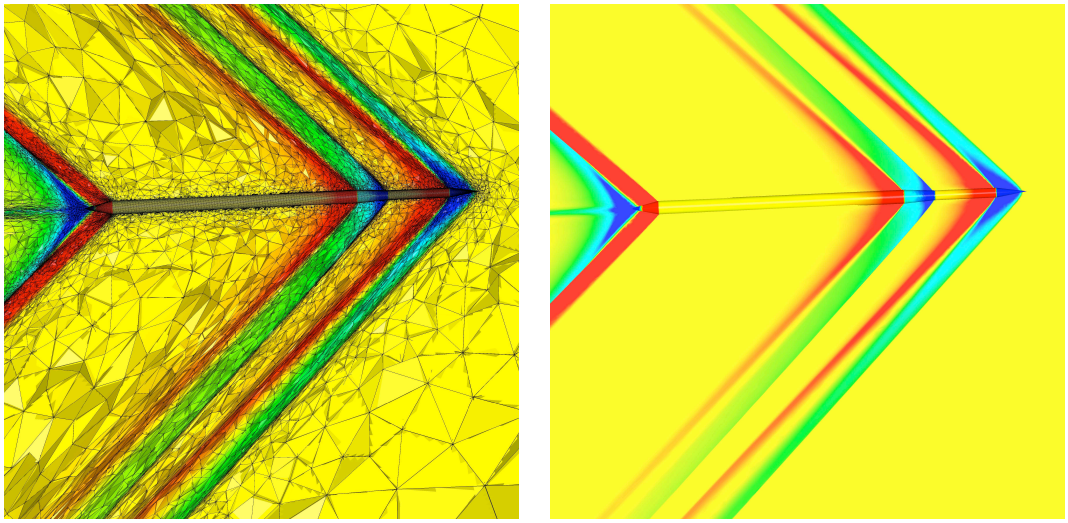

Figure 7: *A close view of the final adpated mesh and the solution of case 5.*

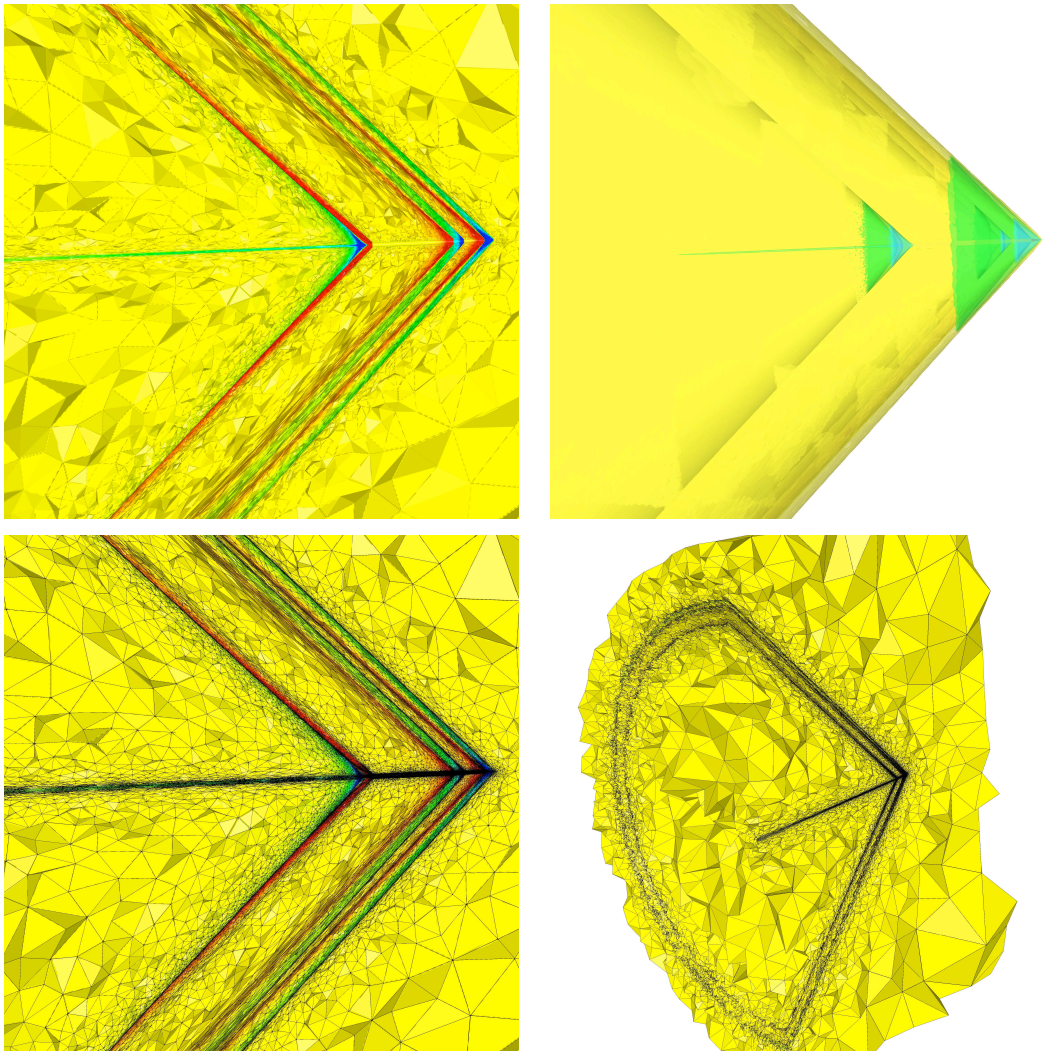

Figure 8: *Final adpated meshes and solution for case 5. Top, Mach number iso-values and iso-surfaces in a plane parallel to the flow. Bottom, view of the anisotropic adapted mesh.*

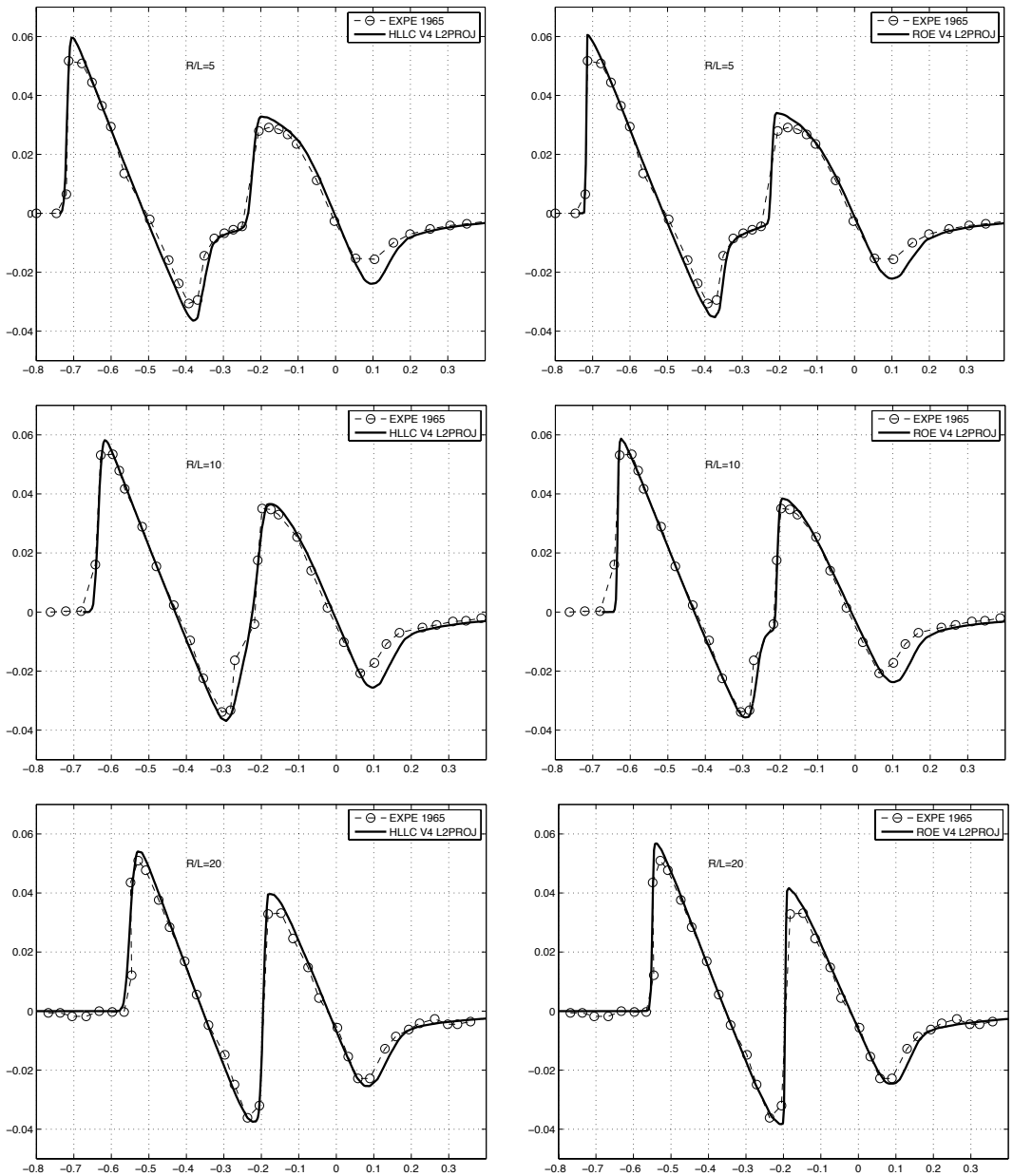

Figure 9: *Comparison between HLLC (left) and Roe (right) Riemann solvers. In both cases, the V4-scheme and a double* $\mathbf{L}^2$*-projection for the Hessian reconstruction have been used.*

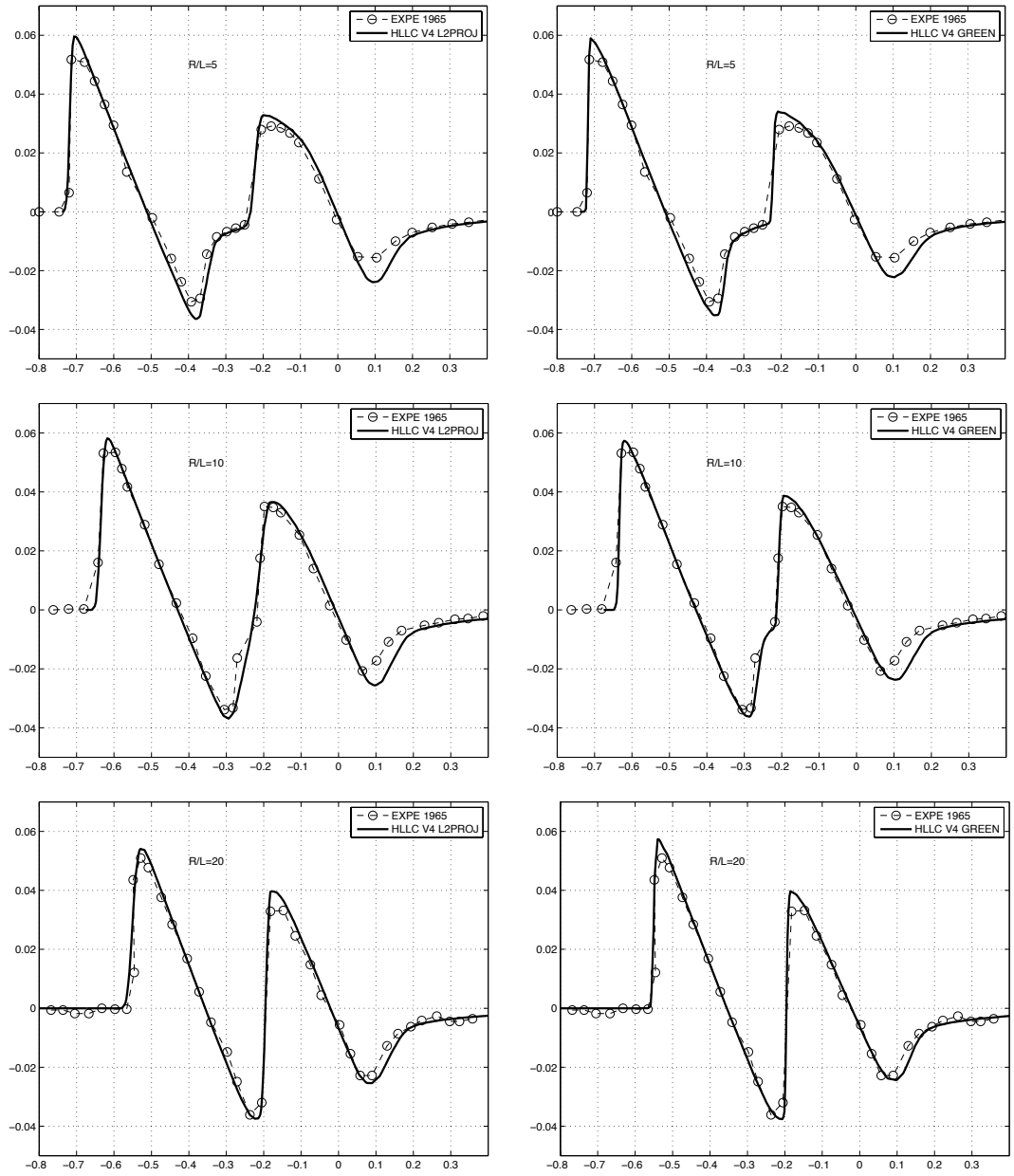

Figure 10: *Comparison between the double $\mathbf{L}^2$-projection (left) and the Green formula (right) for the Hessian reconstruction. In both cases, the V4-scheme with the HLLC Riemann solver have been used.*

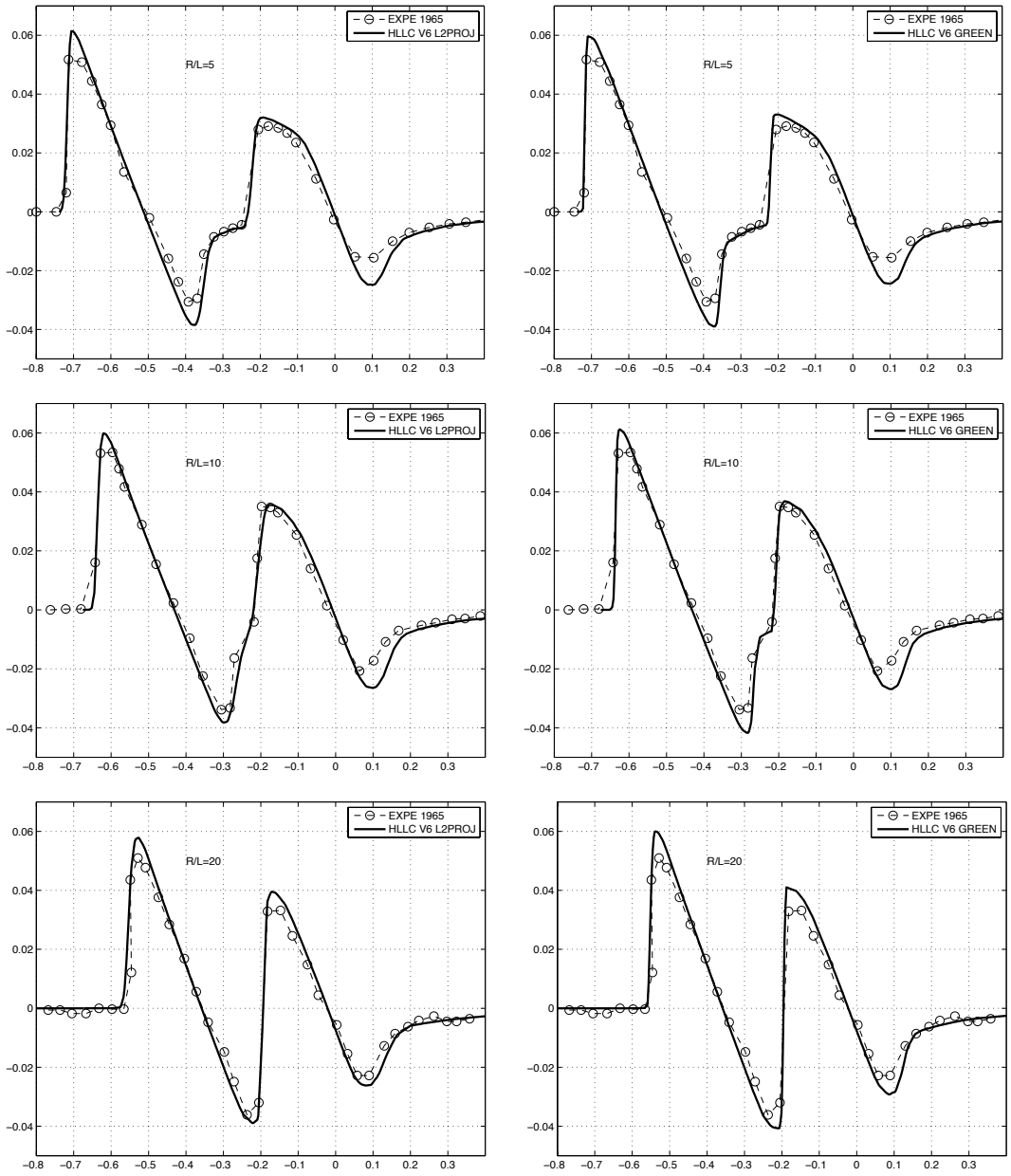

Figure 11: *Comparison between the double $\mathbf{L}^2$-projection (left) and the Green formula (right) for the Hessian reconstruction. In both cases, the V6-scheme with the HLLC Riemann solver have been used.*

4 Sonic boom modeling

Due to the complexity of the phenomenon, accurate simulation of sonic boom signals at the ground requires to couple non-linear CFD models and linear acoustic propagation equations. The near-field and mid-field flows are computed by solving the Euler equations with the adaptive techniques presented previously. The pressure distribution obtained under the aircraft in the mid-field region is used to set up the initial conditions for the propagation of the acoustic waves to the ground. This propagation is achieved with a one-dimensional simplified model resulting in the sonic boom signature. However, the coupling is valid only if specific conditions given by the linear supersonic aerodynamic theory are verified. These points are discussed in the following.

4.1 Atmospheric pressure wave propagation

The propagation code uses a ray tracing algorithm based upon the waveform parameter method developed by Thomas [37]. This algorithm propagates the near-field perturbations to the ground in order to get the sonic boom signature. In this approach, the pressure wave is characterized by three parameters (see Figure 12):

- m_i the slope of pressure waveform segment i
- Δp_i the pressure rise across shock at the juncture of pressure waveform segment i and $i-1$
- λ_i the time duration of pressure waveform segment i.

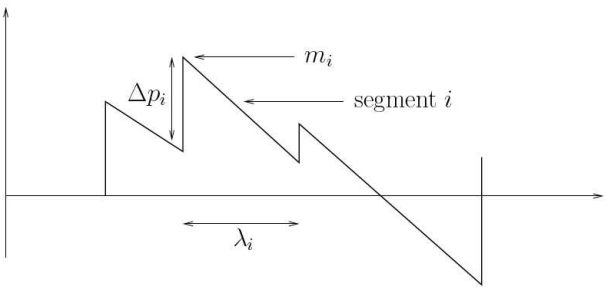

Figure 12: *Illustration of the three parameters m_i, Δp_i and λ_i characterizing the pressure wave.*

A system of three ordinary differential equations (ODE), one for each parameter, is solved to propagate the pressure wave in the atmosphere:

$$\left\{ \begin{array}{rcl} \dfrac{dm_i}{dt} & = & C_1\, m_i^2 + C_2\, m_i\,, \\ \dfrac{d\Delta p_i}{dt} & = & \dfrac{1}{2}\, C_1 \Delta p_i (m_i + m_{i-1}) + C_2 \Delta p_i\,, \\ \dfrac{d\lambda_i}{dt} & = & -\dfrac{1}{2}\, C_1 (\Delta p_i + \Delta p_{i+1}) - C_1 m_i \lambda_i\,, \end{array} \right. \tag{10}$$

with notations:

$$C_1 = \frac{\gamma+1}{2\gamma}\,\frac{c}{p\,a_n} \quad \text{and} \quad C_2 = \frac{1}{2}\left(\frac{3}{c}\frac{dc}{dt} + \frac{1}{\rho(z)}\frac{d\rho}{dt} - \frac{2}{a_n}\frac{da_n}{dt} - \frac{1}{A}\frac{dA}{dt}\right),$$

where c, ρ and p are the air ambient sound speed, density and pressure, respectively. We have denoted by a_n the speed at which a wave propagates along the acoustic ray cone and A the acoustic ray tube area as cut by the waveform (*i.e.,* the Mach cone), cf. Figure 13. All these quantities are functions of the altitude. The speed at which a wave propagates along the acoustic ray cone is given by $a_n = c + \mathbf{v}.\mathbf{n}$ where $\mathbf{v}$ is the wind velocity and $\mathbf{n}$ the wavefront unit normal. If the wind velocity is assumed to be zero then we have $a_n = c$.

Acoustic rays are emitted by the aircraft and propagate orthogonally to the wavefronts. They represent the paths (*i.e.,* the geodesics) along which the acoustic disturbance propagates in the atmosphere. They form the *ray tube* or *ray cone*, cf. Figure 13. The initial direction of a ray is given by the ray cone near the aircraft which is orthogonal to the Mach cone. To compute the ray tube area, four rays are selected, separated by a time increment and an azimuthal increment. The initial directions of these rays are governed by the aircraft flight parameters and the considered azimuth. With these initial conditions, ray paths may be traced. Rays are traced by direct numerical integration of the eiconal. All four rays are traced in this way and ray tube area are computed by numerical differencing. Detailed formulae to compute wavefront unit normal and ray tube area are given in [17]. In this study, we only analyze sonic boom signature for an angle of emission (or azimuthal angle) of acoustical rays equal to zero.

The atmosphere has to be defined to evaluate these quantities. In other words, the temperature and the pressure evolution as a function of the altitude has to be specified. Here, we consider the ICAO Standard atmosphere [20]. This atmosphere is accurately represented by the following analytical functions:

$$\begin{array}{rcl} T(z) & = & \max(T_{gnd} - 6.5\,z\,,\, 216.65)\,, \\ p(z) & = & \left\{ \begin{array}{ll} p_{gnd}\left(1 - \dfrac{6.50\,z}{T_{gnd}}\right)^{5.26} & \text{if } 0\,km < z < 12.25\,km\,, \\ p_{gnd}\left(1 - \dfrac{3.04\,z}{T_{gnd}}\right)^{12.26} & \text{if } 12.25\,km < z < 30\,km\,, \end{array} \right. \end{array}$$

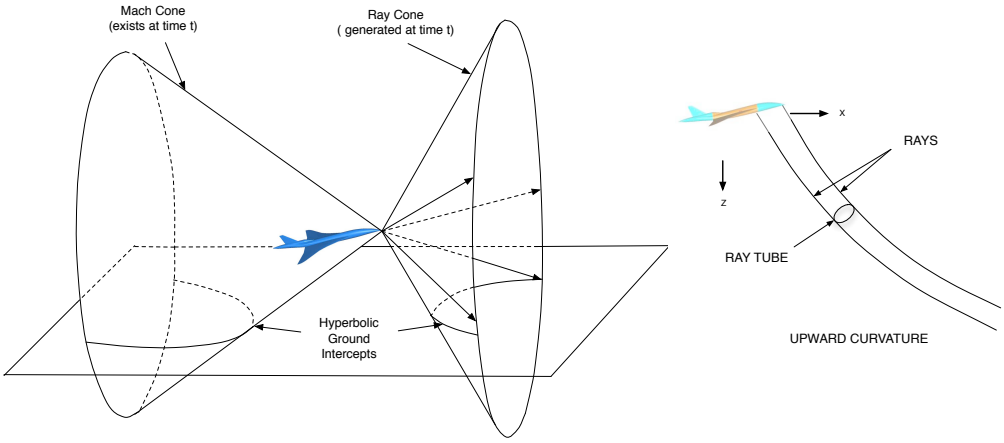

Figure 13: *Left, definition of the ray cone which represents the paths along which the acoustic disturbance propagates. Right, definition of ray tube and its area.*

where $T_{gnd} = 288.15\,K$ and $p_{gnd} = 101\,300\,Pa$ are the temperature in Kelvin and pressure in Pascal at the ground, respectively. Moreover, we assume that the air is following the perfect gas rule. A complementary hypothesis is made by assuming that there is no-wind between the flight altitude and the ground.

To solve this system, the three ordinary differential equations of System (10) are integrated in time by considering sufficiently small time steps in order to be able to assume that variables C_1 and C_2 are constants. Moreover, the time steps must be adequately truncated throughout the resolution. Indeed, as the wave propagates down the ray path, shocks will coalesce to form a new one. When this occurs one or more of the λ_i will go to zero. When one of the λ_i does go to zero somewhere between two points on the ray path, the associated segment is suppressed and the waveform parameters must be redefined. The ground reflexion is taken into account by a reflexion coefficient equal to 1, thus implying pressure doubling at the ground surface (altitude 0) because of the reflexion.

4.2 Coupling CFD and wave propagation

Simulation of the sonic boom signal at the ground requires to couple CFD models and acoustic propagation equations. The mid-field solution of the Euler code is used as initialization. More precisely, a pressure distribution is extracted under the aircraft in the mid-field region to set up initial conditions for the propagation. The extraction is presented in the next paragraph. To ensure a valid coupling, the solution where the initial signal is extracted must verify the Whitham linear supersonic aerodynamic theory. Those conditions are explained in the last paragraph.

Let us first introduce the utilized nomenclature. We denote by:

- α the angle of attack of the aircraft

- M the Mach number
- p the acoustical pressure and p_∞ the atmospherical pressure
- β is the Mach cone angle with the flow direction defined by : $\sin\,\beta = \dfrac{1}{M}$
- L is the length of the aircraft
- R the distance of the observation point from the line parallel to the flow direction (or the ground) going through the nose of the aircraft
- θ is the azimuthal angle or the emission angle

In practice, the distance from the aircraft is generally expressed with the ratio R/L.

Source signature extraction. Assuming that the aircraft is flying along the x-axis from positive to negative x, the extraction line at distance 0, or $R/L = 0$, is the line going through the nose of the aircraft with an angle of α in the symmetric plane Oxz. In other words, a line parallel to the flow direction going through the nose of the aircraft. This line is defined by its two extrema:

$$\left\{\begin{array}{lcl} x_0 &=& x_{jet} - l_{front}\,cos\,\alpha \\ y_0 &=& y_{jet} \\ z_0 &=& z_{jet} - l_{front}\,sin\,\alpha \end{array}\right. \quad \text{and} \quad \left\{\begin{array}{lcl} x_1 &=& x_{jet} + (L + l_{back})\,\cos\,\alpha \\ y_1 &=& y_{jet} \\ z_1 &=& z_{jet} + (L + l_{back})\,\sin\,\alpha \end{array}\right.$$

where $P_{jet} = (x_{jet}, y_{jet}, z_{jet})$ is the nose of the aircraft and, l_{front} and l_{back} are the length of the line before the nose and after the tail of the aircraft, respectively. The extraction line at a given distance R/L is obtained by translating it along the Mach cone:

$$\left\{\begin{array}{lcl} x_i^{R/L} &=& x_i + R\,\dfrac{\cos\,(\beta-\alpha)}{\sin\,\beta} \\ y_i^{R/L} &=& y_i \\ z_i^{R/L} &=& z_i - R\,\dfrac{\sin\,(\beta-\alpha)}{\sin\,\beta} \end{array}\right. \quad \text{for } i = 0, 1\,.$$

Finally, the extraction line at a given R/L and a given azimuthal angle θ is defined by:

$$\left\{\begin{array}{lcl} x_i^{R/L,\theta} &=& x_i + R\,\cos\,\theta\,\sin\,\alpha + R\,\dfrac{\cos\,\alpha}{\tan\,\beta} \\ y_i^{R/L,\theta} &=& y_i + R\,\sin\,\theta \\ z_i^{R/L,\theta} &=& z_i - R\,\cos\,\theta\,\cos\,\alpha + R\,\dfrac{\sin\,\alpha}{\tan\,\beta} \end{array}\right. \quad \text{for } i = 0, 1\,.$$

In all this study, we only consider extraction line at azimuthal angle 0.

The pressure variation along the extraction line is used as an initial input for the propagation code. In our implementation, this line corresponds to a uniform *a posteriori* discretization along the flight path. The pressure values on this discretization are obtained by interpolating linearly the aerodynamic near-field pressure. To this end, each point of the line is localized in the tetrahedral CFD mesh, *i.e.,* we find the tetrahedron to which it belongs. In our approach, the segment discretization

is finer than the one used in the CFD computation. Practically, the initial input for the propagation code is the pressure variation:

$$\delta p = \frac{p - p_\infty}{p_\infty} .$$

Validity of the coupling. The flow near the aircraft is three-dimensional and non-linear in nature whereas the propagation is a linear one-dimensional model. The coupling between these two models becomes valid if some assumptions are verified, meaning that the mid-field pressure signal can be used (as a F-function) to initialize the propagation. As stated in [30], there is a matching radius between the source function and the propagation extrapolation. The assumption, that has not been rigorously verified, is that the use of the pressure signal become valid when the flow field does no more contain any crossflow components. In other words, the flow field is locally axisymmetric and it has no more non-linear effect. As crossflow components are very significant at small radii but are less at larger distances. The pressure signal has to be extracted in the mid-field far enough from the aircraft to respect such condition. This is a necessary condition to take all the elements of the aircraft geometry (body, wings,...) into account in the sonic boom signature.

This condition can be verified according to the linear supersonic aerodynamic theory. Experimentally (cf. see for instance the results of Section 3.3), the law variation of the pressure front δp decreases proportionally to $R^{-\frac{3}{4}}$ (equivalently $(R/L)^{-\frac{3}{4}}$) while the duration of the wave grows in $R^{\frac{1}{4}}$ (see also Section 3.3). The pressure decrease law tends toward R^{-1} near the mobile where high non-linearities occur. And, this law tends toward $R^{-\frac{1}{2}}$ when the non-linear effect become negligible. To summarize, the CFD flow field is considered converged and locally axisymmetric if the pressure variation tends to decrease proportionally to $(R/L)^{-\frac{1}{2}}$.

Nevertheless, such a condition has to be verified carefully. Indeed, a non-linearity diffusing behavior may appear in the solution due to the numerical dissipation of the flow solver. In particular, if the CFD mesh is not refined enough, shock waves will be diffused throughout their propagation and non-linearities will be removed.

As a consequence, multi-scales anisotropic mesh adaptation can remedy this issue as it controls globally the mesh sizes and guarantees a coherent numerical dissipation in the whole computational domain. In order to certify the propagation, we propose to analyze the convergence of the sonic boom signature with respect to the extraction distance.

5 Studying the sonic boom of several SSBJs

In this section, we study and compare three supersonic business jet (SSBJ) geometries that have been provided by Dassault Aviation during the HISAC european project [18].

The first aircraft, cf. Figure 16 top, is a low drag jet. In the following, we will refer to as the **low drag** jet. This geometry is the simplest one. In particular, the engines have not been integrated while it is known that they have a significant impact on the sonic boom. The length of this jet is $L = 37$ meters and it has a wing span of 17 meters. The surface mesh accuracy varies between 1 millimeter and 30 centimeters.

The second aircraft is a low-boom-shaped jet. The geometry is more complex than the previous one. Notably, the engine have been integrated. We notice that the engine have been integrated over the fuselage to minimize the impact of the nacelles on the sonic boom. The aircraft length is $L = 42$ meters and it has a wing span of 20 meters. The surface mesh accuracy varies between 0.2 millimeters and 12 centimeters. This represents already a size variation of five orders of magnitude with respect to the aircraft size, and this only for the surface mesh ! Two versions of this jet are studied. The difference between the two shapes is the wing. The first one has flat wing, it is represented in Figure 16 (middle). We name it **low boom** jet. For the second shape, the wing has a double dihedral angle, Figure 16 (bottom). The first dihedral angle is at the junction of the wing and the fuselage. The second one is where the wing swept angle change. The wing differences are clearly visible in Figure 20. This second shape will be refer as the **low boom + dihedral** jet. With this geometry, wing dihedral angles effectiveness on the sonic boom will be analyzed

The computational domain is a cylinder of 2.25 kilometers length and 1.5 kilometers diameter. This represents a scale factor of 10^7 if the size of the domain is compared to the maximal accuracy of the low boom jet surface mesh. This domain size enables pressure signature in the mid-field to be obtained up to $R/L = 19$ for the low drag jet and $R/L = 16$ for both low boom models.

This section is outlined as follow. First, the parameters of the study are given. Then, the global orders of convergence of each simulation are presented and the CFD results obtained for the near-field and mid-field are discussed. In a fourth subsection, we analyze the convergence of the pressure signals with respect to the ratio R/L and we specify the distance at which the coupling between CFD and propagation becomes valid. The sonic boom signature convergence is also studied. Finally, the acoustic signals of each geometry are compared.

In the results description, we do not provide the physical values obtained for the drag, the mid-field pressure signals and the sonic booms for confidentiality reason. We will only provide relative values scaled on the results obtained for the low drag jet.

5.1 Study parameters

The same simulation parameters are considered for the three SSBJ geometries. The flight conditions are a supersonic cruise speed of Mach 1.6 at an altitude of $13\,680$ meters ($45\,000$ feet). In order to be able to compare the sonic boom associated to each jet, it is fundamental to perform the computations at the same lift. Indeed, the sonic boom (the shock waves) is a consequence of the lift effect. In this study, the cruise lift has been set to $C_l = 0.115$ by Dassault Aviation. The angle of attack for each aircraft is then set such that this lift is attained. In each case, the angle of attack of the simulation is defined on the initial mesh which is accurate close to the aircraft. These initial meshes are composed of almost $330\,000$ vertices for the low drag jet and $550\,000$ vertices for the low boom jets. The obtained angles of attack of each aircraft are near to 3 degrees.

As regards the finite volume solver, we have specified the HLLC Riemann solver, the V6-scheme with the Dervieux limiter and for the temporal integration the 5-stage order-2 SSPRK scheme. For the low boom jets, the engine data for the boundary conditions have been specified by Dassault Aviation. The lift and drag coefficient are computed according to the reference data of each geometry.

The multi-scales mesh adaptation considers a control of the interpolation error in $\mathbf{L}^2$ norm of the local Mach number. The local Mach number has been selected as it is really representative of supersonic flows. We have deliberately chosen to do not adapt the aircrafts surface meshes. Indeed, the provided surface meshes are very accurate and are of high quality for the computations. A mesh gradation of 2.5 has been set [1]. A total of 32 adaptations have been performed. The mesh adaptation loop is split into 4 steps of 8 adaptations. At each step, the couple mesh-solution is algorithmically converged at a fixed complexity. This complexity is multiplied by two between two steps. This strategy has two main advantages. First, it enables us to perform a convergence study of the whole solution as a series of couple mesh-solution with an increasing accuracy is obtained. Second, considering an increasing dynamic complexity level accelerates the convergence of the whole process. We have fixed the following complexities:

$$[100\,000, 200\,000, 400\,000, 800\,000],$$

which give meshes the size of which is almost 0.8, 1.7, 4 and 9 millions of vertices. The simulations were run on a four-processors 64-bits Mac Pro with an Intel Core 2 chipsets with a clockspeed of 2.8 GHz with 16 Gb of RAM. The total CPU time for these simulations is approximately 4 days

5.2 Computations validation

To validate the computations, the global convergence order of each geometry is analyzed with respect to a reference solution. In each case, the reference solution is the final solution obtained on the finest adapted mesh for a complexity equal to $800\,000$. The convergence is computed in $\mathbf{L}^2$ norm on the Mach number which is the variable used for the mesh adaptation. For the low drag, the low boom and the low boom + dihedral jets, we obtained convergence orders equal to $2.$, 1.65 and 1.65, respectively. The convergence plots are given in Figure 14.

For the simplest geometry, the low drag aircraft, the theoretical order has been attained. As regards the low boom geometries, the obtained convergence order is less than two. Two hypothesizes are envisaged to explain these results. First, the final solutions for the last three steps (*i.e.,* at adaptations 16, 24 and 32) are not numerically fully converged for CPU time reason. Indeed, these geometries are really more complex than the low drag one, notably engine boundary conditions are employed. The second hypothesis is that there is a loss of convergence order due to the mesh gradation procedure. But, these hypothesizes still have to be verified.

5.3 Near-field and mid-field results

For each computation, very accurate results in the whole computational domain are obtained for the final adapted meshes containing almost 9 millions vertices. In particular, the accuracy of the tetrahedral meshes have reached the surface meshes accuracy and the refinements have been propagated in the whole computational domain. The sizes of the final meshes are summarized in Table 2.

This is illustrated in Figure 15 where the mach cones of the low boom + dihedral and the low drag SSBJs are depicted. The numerical dissipation of the flow solver has been drastically reduced thanks to the anisotropic mesh adaptation. The shock waves have accurately propagated in the whole computational domain, more than one kilometer below the SSBJs.

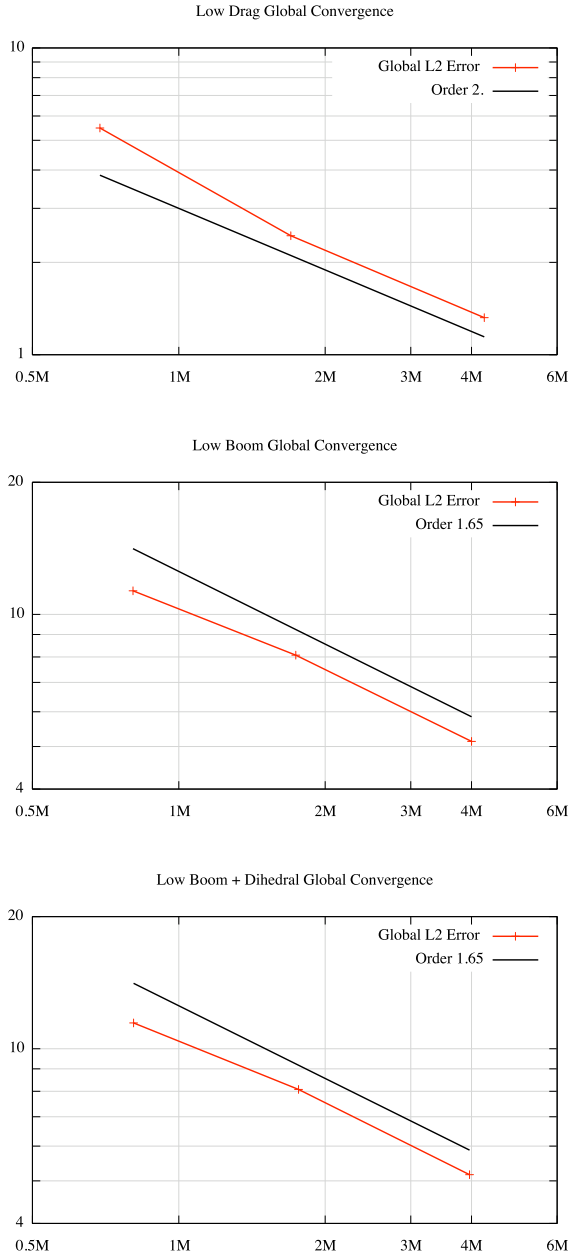

Figure 14: Global mesh convergence order for each SSBJ. From top to bottom, we obtain an order of 2. for the low drag jet, 1.65 for the low boom jet and 1.65 for the low boom + dihedral jet.

The surface meshes and the associated solutions of each SSBJ are shown in Figure 16. One can see the difference in the shock position on the wing due to the wing dihedral angle for the low boom configuration.

The Figure 17 illustrates the Mach number iso-values and the final adapted mesh in the symmetry plane $0xz$. We notice that the shock waves and the anisotropic refinements have been propagated in the whole domain without any dissipation. We also remark the very accurate capture inside the mesh of the shock waves at the inlet and the exhaust of the engines. This points out the multi-scales behavior of the mesh adaptation approach.

Cut planes of the volume meshes under the SSBJs are presented in Figure 18. This view shows that each element of the geometry emits its own shock waves. The focalization of shocks during their propagation is also illustrated inside the mesh.

The Figures 19 and 20 are two views of the final mesh and the final solution of each configuration in a cut plane behind the jet orthogonally to its path. They illustrate the mesh anisotropy along shocks and the multi-scales effects with the capture of vortices in the wake. They also point out the great complexity of the physical phenomenon and of the mesh refinement. This demonstrates the necessity to use a fully automatic mesh adaptive method.

Geometry	$\mathcal{T}_{final}$ # vertices	$\mathcal{T}_{final}$ # tetrahedra
Low drag	9 465 835	56 568 966
Low boom	9 077 197	53 842 961
Low boom + dihedral	9 083 531	53 884 863

Table 2: Number of vertices and tetrahedra for the final adapted meshes.

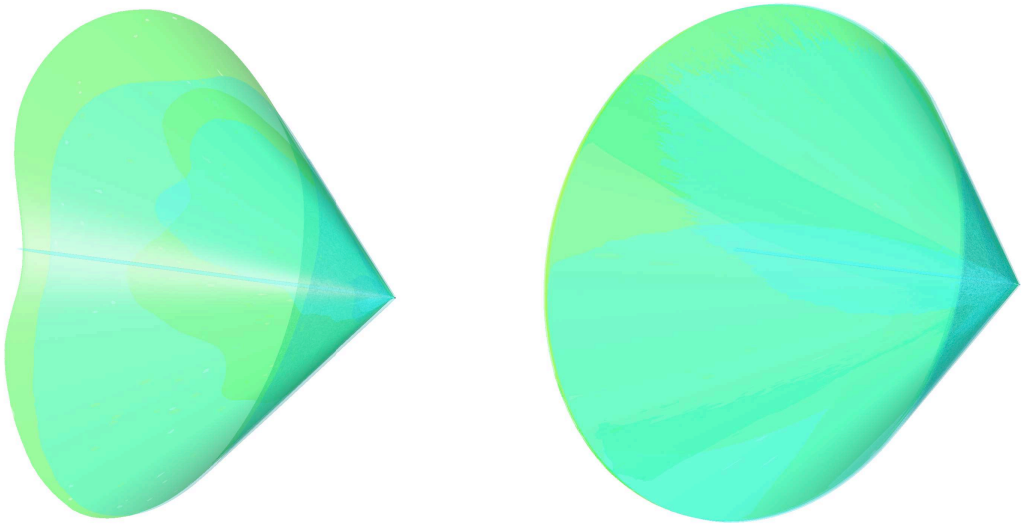

Figure 15: Left, the Mach cone emitted by the low boom + dihedral SSBJ. Right, the Mach cone emitted by the low drag SSBJ. The maximal Mach cone diameter is 1.25 kilometers.

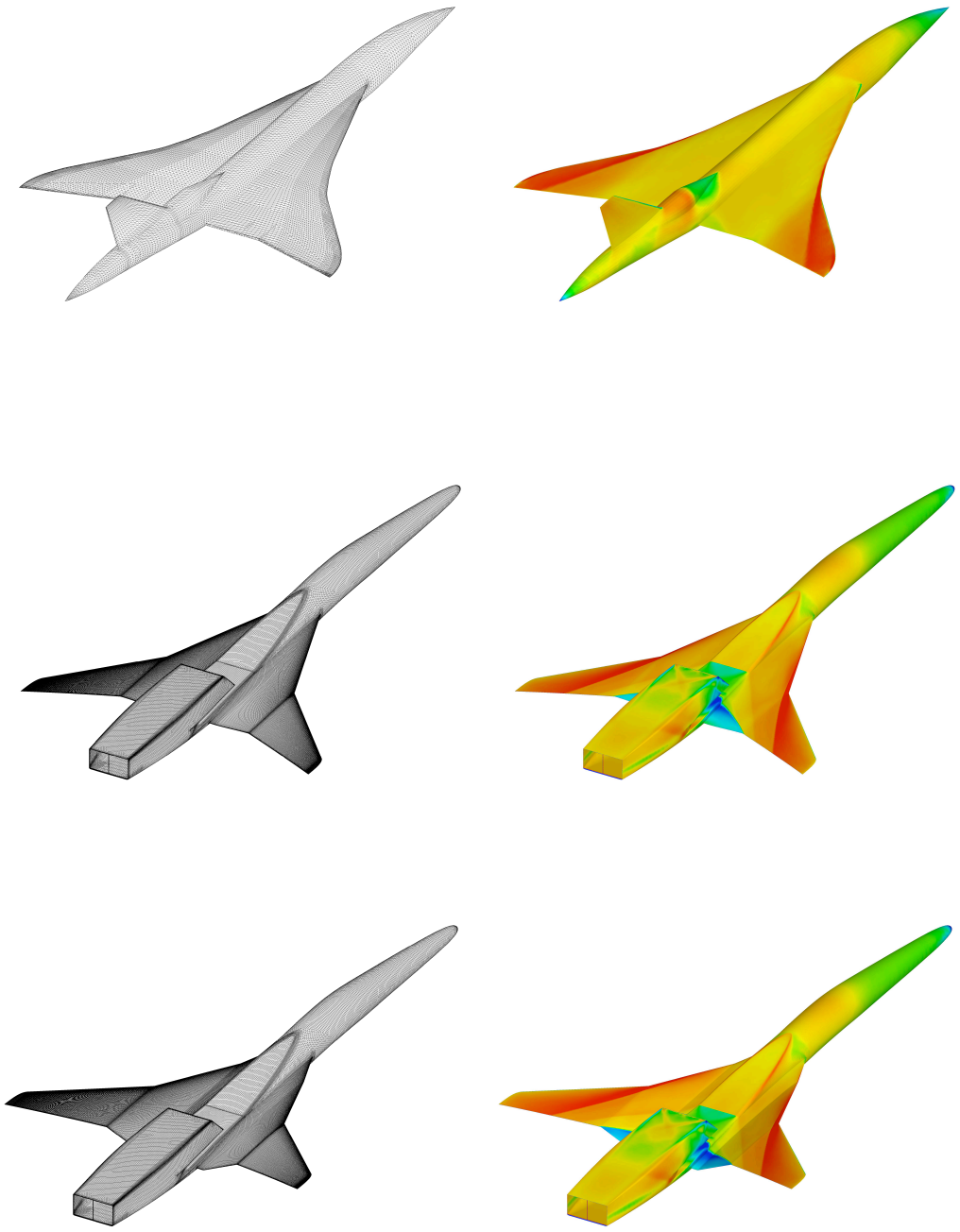

Figure 16: From top to bottom, the three studied configurations: the low drag jet, the low boom jet and the low boom + dihedral jet. Left, the surface meshes, and right, the Mach number iso-values.

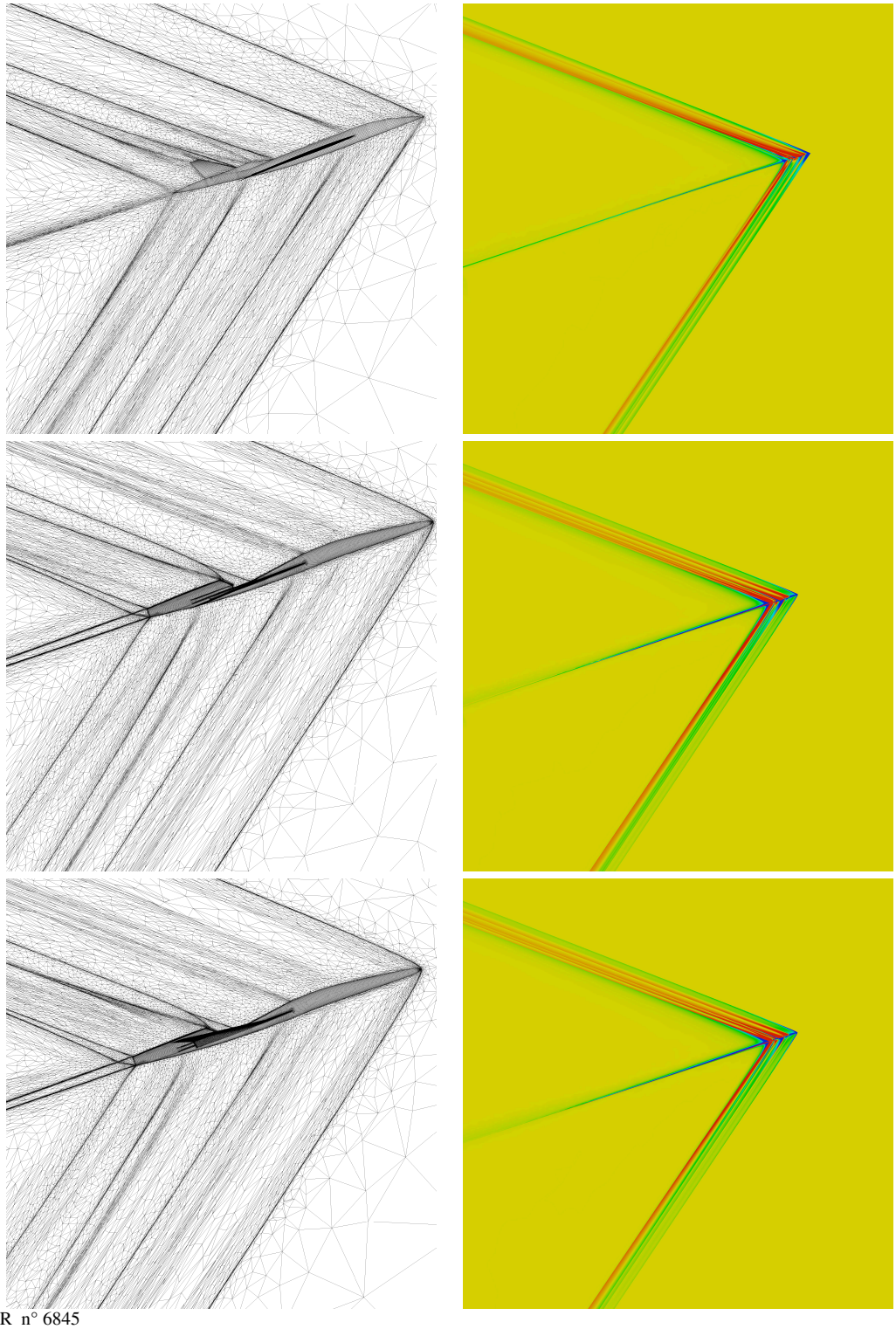

Figure 17: From top to bottom, the low drag jet, the low boom jet and the low boom + dihedral jet. Left, view of the adapted volume mesh through the cut plane along $0xz$, and right, the associated Mach number.

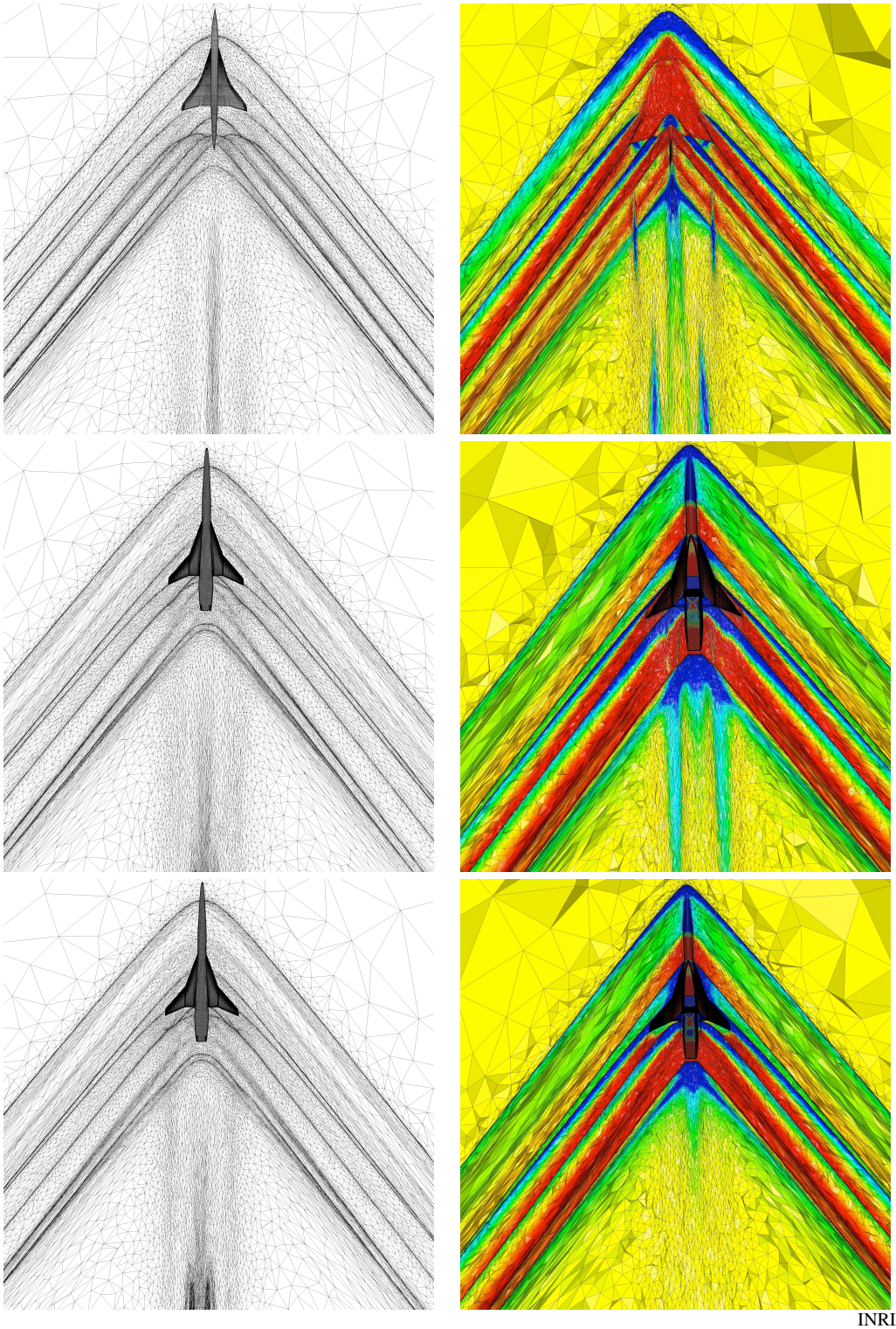

Figure 18: From top to bottom, the low drag jet, the low boom jet and the low boom + dihedral jet. Left, view of the adapted volume mesh through the cut plane along $0xy$, and right, the associated Mach number.

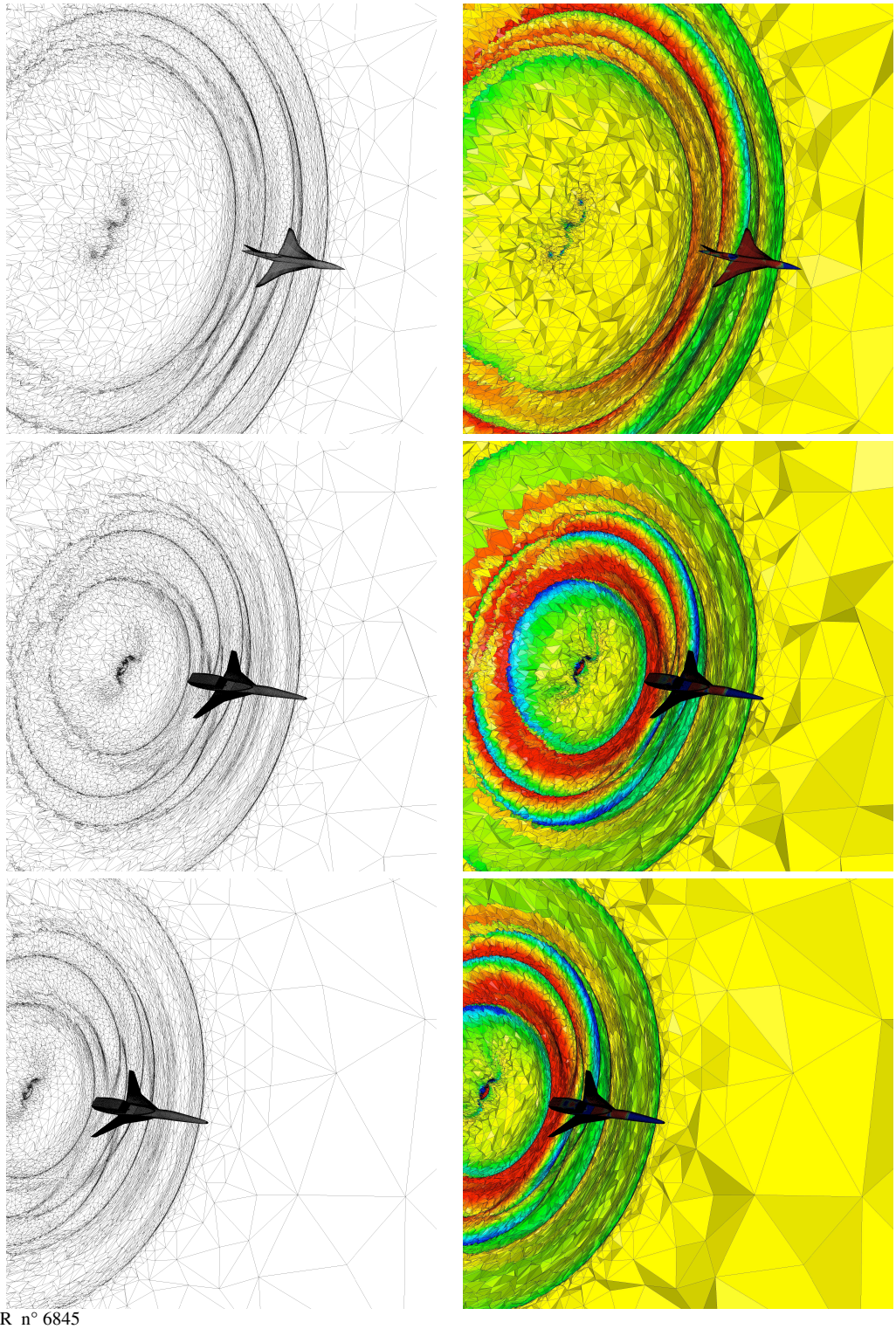

Figure 19: From top to bottom, the low drag jet, the low boom jet and the low boom + dihedral jet. Left, view of the adapted volume mesh through the cut plane along $0yz$, and right, the associated Mach number.

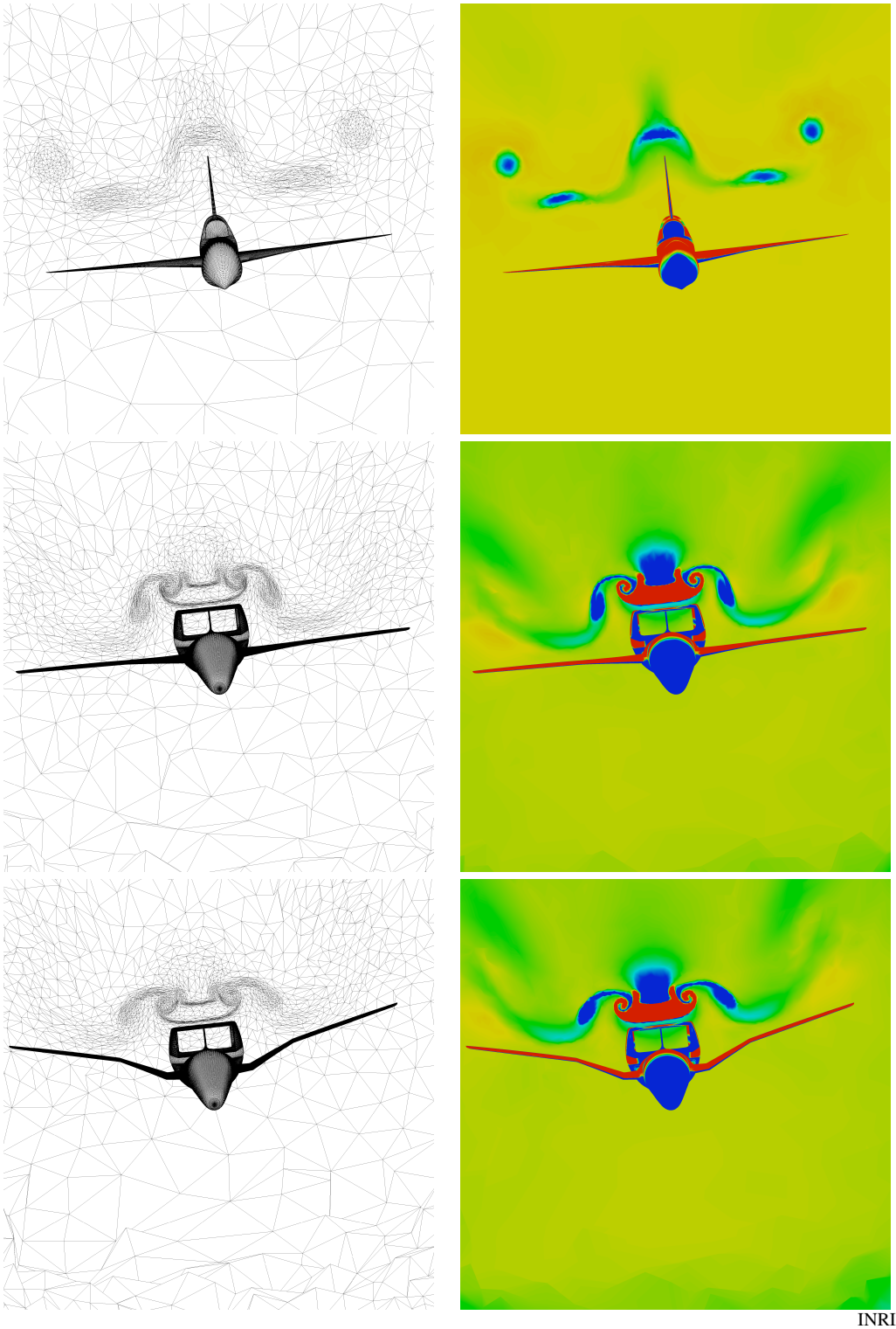

INRIA

Figure 20: From top to bottom, the low drag jet, the low boom jet and the low boom + dihedral jet. Left, view of the adapted volume mesh through the cut plane along $0xy$, and right, the associated Mach number.

5.4 Mid-field and sonic boom convergence

Figures 21, 22 and 23 display on the left the pressure signatures for the near-field ($R/L = 1$) and the mid-field (R/L from 5 to 19) for each configuration and, on the right, the associated sonic boom signal, *i.e.,* the boom issued from those pressure signatures. In the following, we will designate by mid-field the pressure signature for R/L from 1 to 19. The mid-field signatures represent $\sqrt{\frac{R}{L}}\,\frac{p-p_\infty}{p_\infty}$ function of the position in meters. The sonic boom plots represent the pressure in Pascal function of the time in milliseconds.

The top and middle plots show the convergence of the acoustic signal in the mid-field, in the sense that the decrease law of the pressure become of the order of $\sqrt{R/L}$. They also illustrate the convergence of the associated sonic boom with respect to R/L. These plots provide an estimation of the required matching radius for each geometry, in other words, the distance from which the crossflow (non-linear) effects become negligible.

For all cases, we do not obtain a boom shape which is a N-wave, but a signal at the ground with three shocks. There is always two shock in the front. The first one is due to the nose of the SSBJ and the second to the wings. The large discrepancy of the pressure signal shape in the mid-field (from $R/L = 1$ to 19 for the low drag jet and from $R/L = 1$ to 16 for the low boom jets) implies a large disparity of the ground sonic boom with respect to the extraction distance. We observe a convergence of the pressure signals and of the booms from $R/L = 6$ for the low drag jet and from $R/L = 11$ for the low boom jets. Indeed, the low boom configurations are more complicated and generates more non-linearities.

The convergence during the mesh adaptation process of the pressure signals at $R/L = 15$ and of the sonic booms propagated from $R/L = 15$ is illustrated in the bottom plots of Figures 21, 22 and 23. The signals of each final solution at a fixed complexity, *i.e.,* at iterations 8, 16, 24 and 32 of the adaptive loop, are compared. We denote by adaptation 1, 2, 3 and 4 the meshes containing almost 0.8, 1.7, 4 and 9 millions vertices.

For the low drag jet, an accurate computation of the boom is nearly attained at adaptation 1 even if the pressure signature in the mid-field is clearly less accurate as compared to the pressure signature at adaptation 4. This smoothing of the shock waves has a small influence on the boom prediction. For the low boom configurations, the accuracy of the mesh at adaptation 2 is required to obtain a good representation of the solution at $R/L = 15$. Else, the first shock of the ground signal is not correctly computed. Notice that at adaptation 2, the region between the first two shocks is not accurately captured.

These observations signify that some scales of the solution, in fact the small details of amplitude, do not influence the sonic boom signature obtained with the Thomas propagation method. However, attention has to be paid with respect to the solution dissipation. If the solution is too dissipated then we will obtained a poor extracted signature. It is thus interesting to note that the dissipation of the numerical scheme obtained on anisotropic adapted meshes seems to have some consistencies during the whole adaptive process by preserving the signal properties.

In conclusion, these simulations have pointed out that it is critical to have a sufficient accurate pressure signal far enough from the SSBJ to obtain a valid coupling between CFD and the propa-

gation code when the Thomas propagation method is used. The matching radius increases with the complexity of the geometry to take into account the crossflow effects. On the other hand, it is not essential to be "very" accurate at the extraction if the dissipation of the signal through its propagation in the mid-field is consistent. Nonetheless, a high accuracy can be required in certain regions of the mid-field to obtain an adequate signal at the extraction.

5.5 Comparison of the different geometries

In this section, we compare the three SSBJ configurations by analyzing:

- the drag
- the mid-field pressure signal at 700 meters under the SSBJ, *i.e.,* $R/L = 18$ for the low drag jet and $R/L = 15.86$ for the low boom jets
- and the sonic boom computed from this extraction.

To handle these comparisons, the values of interest (the drag and the intensity of the three shocks of the boom) are given relatively to the low drag configuration. We set a drag of 1 for the low drag jet and all sonic boom shock amplitude are compared relatively to the first shock of the boom of the low drag jet which is set to an amplitude of 1. The relative results are summarize in Table 3.

We first compare the low drag and the low boom configurations, Figure 24. Then, we analyze the effect of a wing dihedral angle on the sonic boom, Figure 25.

Low drag vs. low boom + dihedral. The mid-field analysis at 700 meters under the SSBJs shows that the low boom shapes reduce significantly the shock due to the nose. On the other hand, the wings shock and the tail shock are slightly higher than those of the low drag jet. These mid-field differences results in a reduction of 36% of the first shock intensity and an increase of 37% and 11% of the amplitude of the second and the third shock for the sonic boom signature. It is surprising to get an increase of 37% of the second shock intensity whereas the mid-field region associated with the wings is quite similar. As regards the shock amplitude increases for the last two shocks, it is important to recall that the low drag jet has no engines that have a notable impact on the sonic boom.

It is interesting to remark the existence of a sinusoidal region between the first and the second shock in the low boom jets sonic boom signatures. It is unusual to see such smooth regions in booms. The current analysis cannot quantify its real impact on the sonic boom. Does it increase the rise time of the second shock knowing that the rise time influence our perception of the sonic boom ?

Wing dihedral effect. The dihedral angle of the wings intrinsically modifies the wings shocks in the mid-field. With this geometry modification, some of lift effects are sent laterally. In the pressure signature at 700 meters, cf. Figure 25, a double shock is obtained with the dihedral instead of a "three-pick" shock. The impact on the sonic boom is to shift the second shock on the right, *i.e.,* it arrives later, and to slightly reduce the amplitude of the last shock: 1.62 instead of 1.65. This is due to the effective length of the low boom + dihedral jet that has been slightly increase thanks to the dihedral. As regards the second shock, the maximal pressure has been a little reduced with

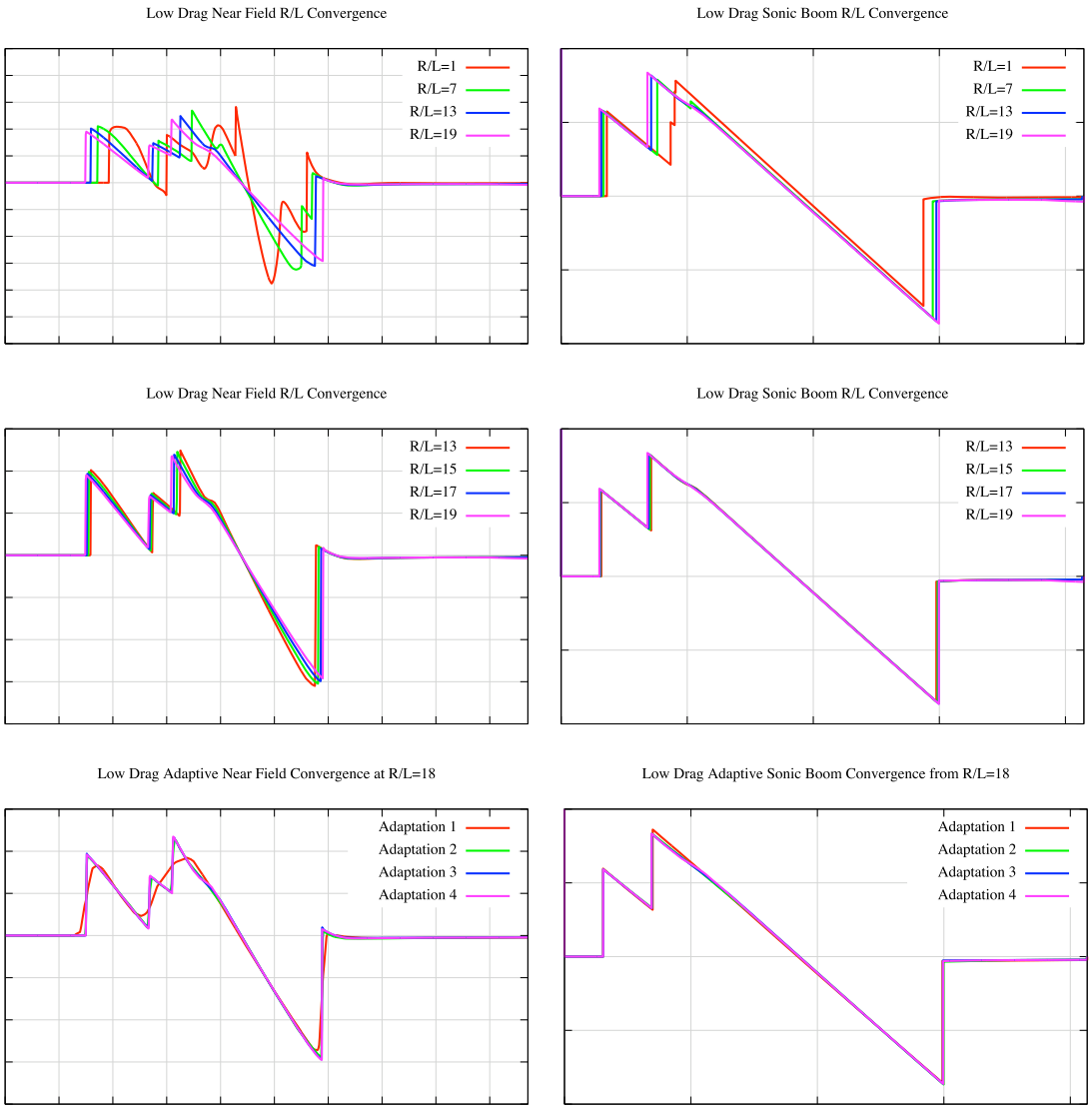

Figure 21: Mid-field pressure signatures (left) and sonic boom signals (right) of the low drag jet. Left, the plots represent $\sqrt{R/L}\,\delta p$ function of the position $\mathbf{x}$. Right, the plots represent the pressure function of the position the time.

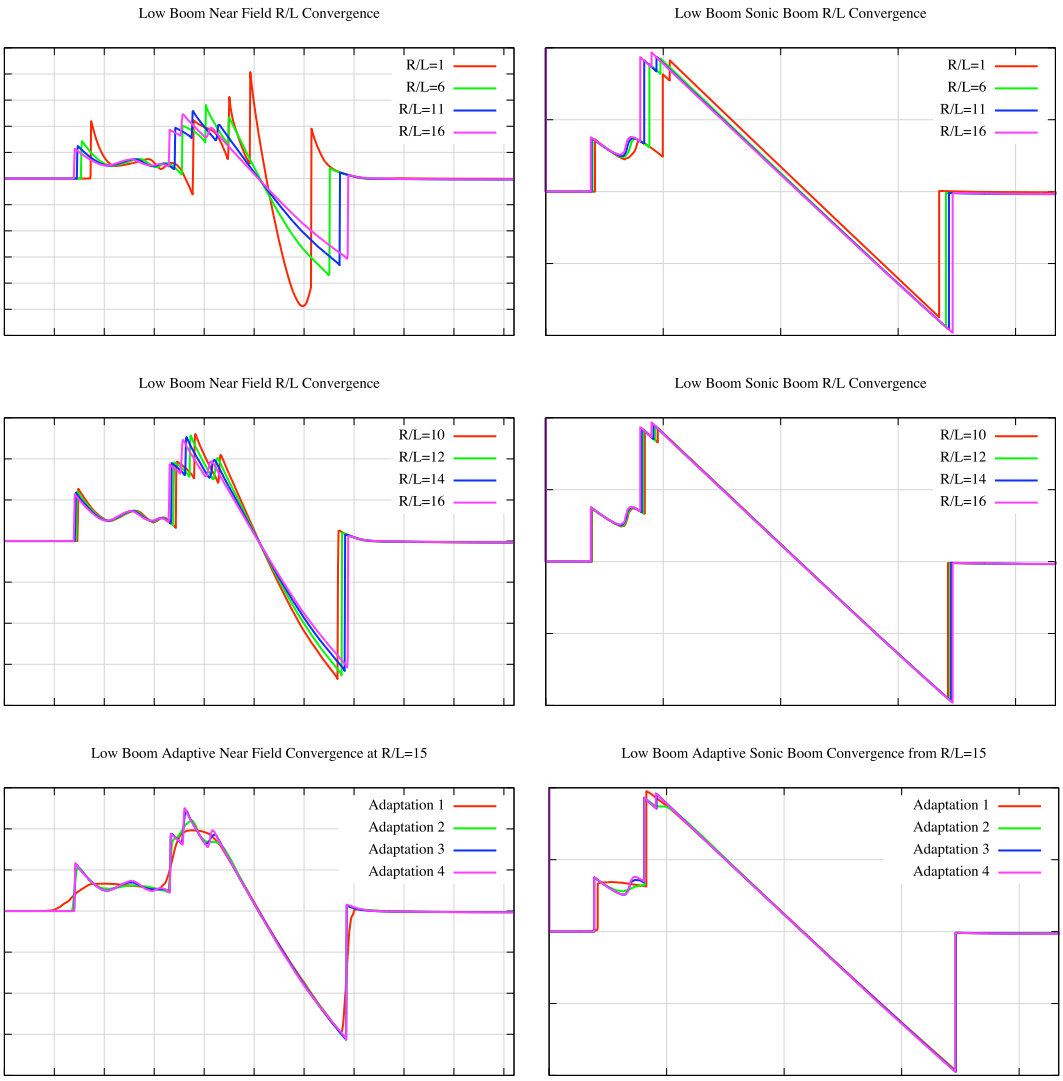

Figure 22: Mid-field pressure signatures (left) and sonic boom signals (right) of the low boom jet. Left, the plots represent $\sqrt{R/L}\,\delta p$ function of the position $\mathbf{x}$. Right, the plots represent the pressure function of the position the time.

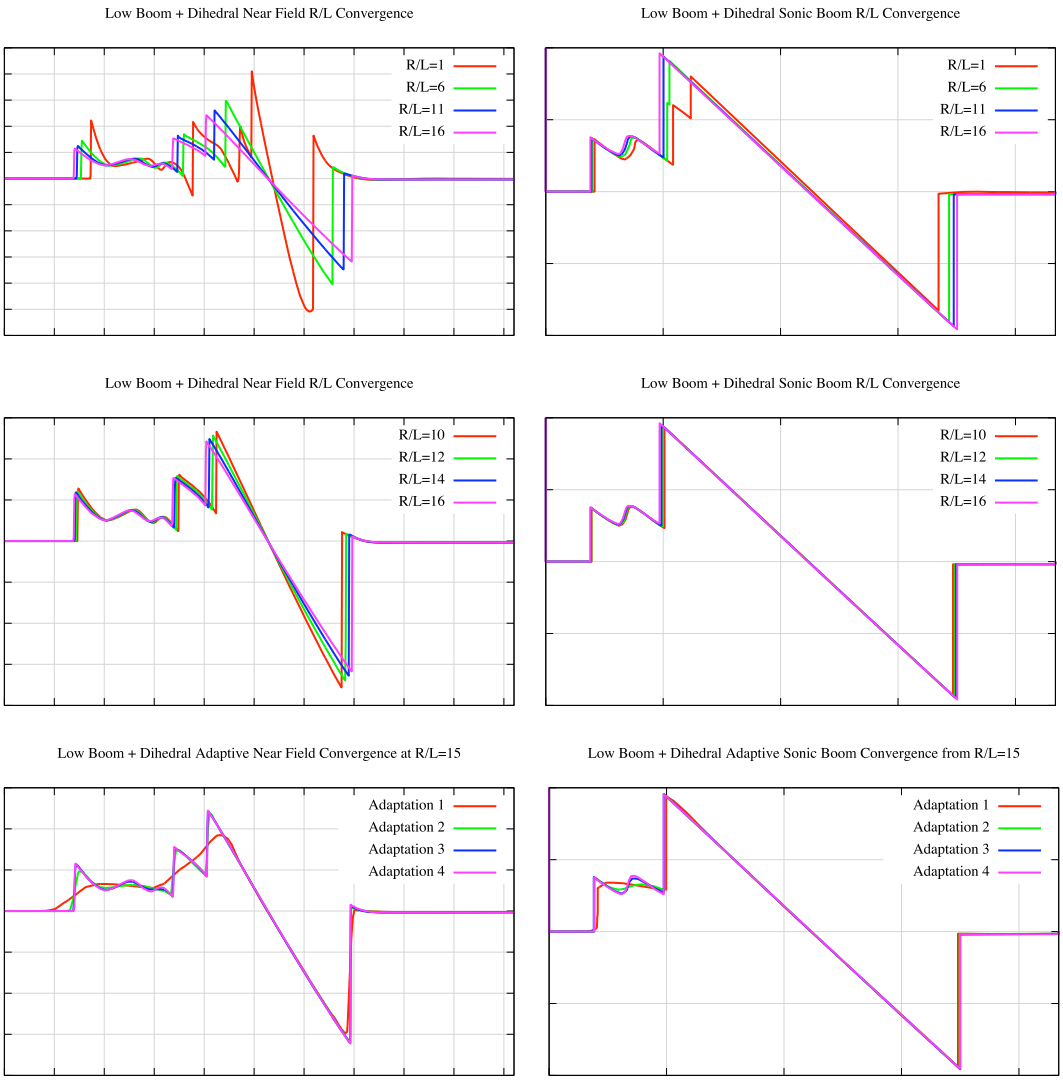

Figure 23: Mid-field pressure signatures (left) and sonic boom signals (right) of the low boom + dihedral jet. Left, the plots represent $\sqrt{R/L}\,\delta p$ function of the position $\mathbf{x}$. Right, the plots represent the pressure function of the position the time.

the dihedral effect. However, because of the smooth sinusoidal region before the second shock, the relative amplitude is higher with the dihedral effect, 1.18 instead of 0.99, as the foot of the shock is at a lower pressure. To sum up, the dihedral effect is positive but it has a slight influence on quietening the sonic boom.

In compensation, the reduction of the first shock of the boom leads to a large augmentation of the drag. A drag of 1.64 and 1.67 are obtained for the low boom and the low boom + dihedral configurations, respectively. This represents an increase of more than 60% illustrating the significant negative impact of a sonic boom optimization on the drag. Nevertheless, the drag of the low drag SSBJ is underestimated as the geometry is not supplied with engines.

Configuration	1^{st} shock	2^{nd} shock	3^{rd} shock	Drag
Low drag	1	0.86	1.46	1
Low boom	0.64	0.99	1.62	1.64
Low boom + dihedral	0.64	1.18	1.56	1.67

Table 3: Relative intensity of the shock waves in the sonic boom signatures for all configurations. The relative drag of each SSBJ is also mentioned.

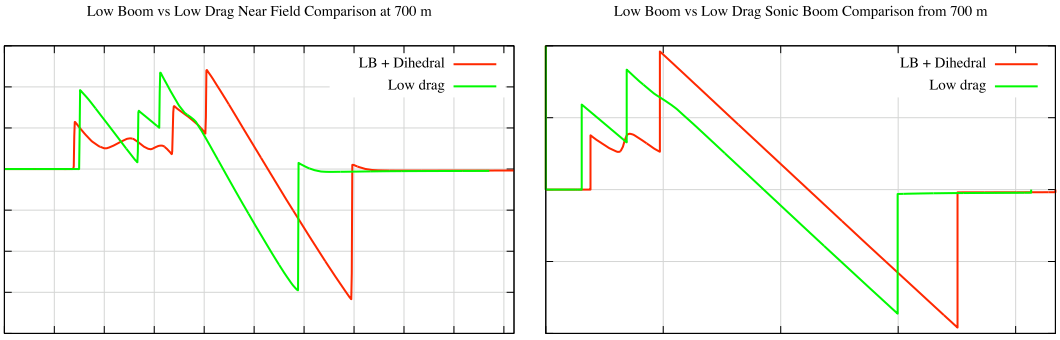

Figure 24: Comparison of the pressure signals and the sonic booms of the low drag jet and the low boom + dihedral jet.

6 Concluding remarks

A high-fidelity sonic boom modeling, coupling adaptive CFD mid-field simulation and ray tracing algorithm for the far-field, has been presented. A crucial point was the use of an adequate anisotropic mesh adaptation approach in order to have a valid coupling by propagating the mid-field signal far

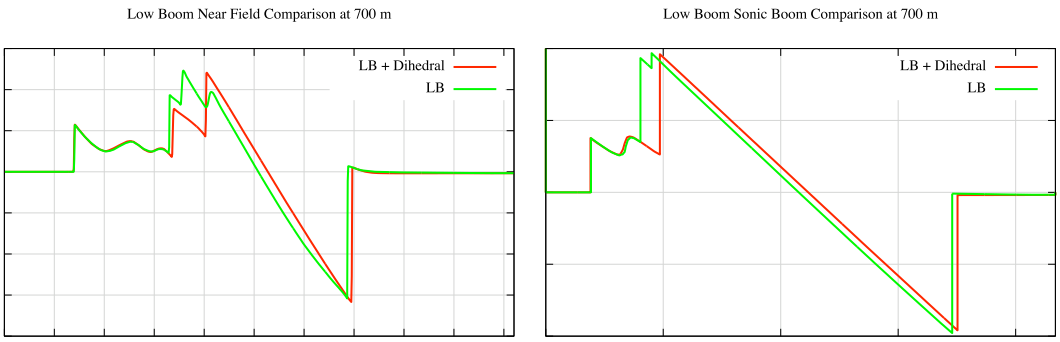

Figure 25: Comparison of the pressure signals and the sonic booms of the low boom + dihedral jet and the low boom jet.

enough from the aircraft and to able to certify the computation by attaining the theoretical mesh convergence order of the solution.

This technology illustrates that CFD on unstructured meshes is no more limited to $R/L = 1$ and that it is now possible with to perform accurate simulations up to $R/L = 20$ and even more.

This approach has been validated on a test case by comparison to experimental data and has been applied successfully to three realistic aircraft configurations. The method was able to propagate anisotropic mesh refinement in whole computational domain without any difficulties to preserve the solution accuracy. It has been demonstrated numerically that, in this case, a mid-field extraction more than $R/L = 10$ (depending on the aircraft geometry complexity) are required to obtain a precise sonic boom signature. Moreover, it has been pointed out that a consistent numerical dissipation is obtained with the flow solver on highly anisotropic adapted meshes. This authorizes accurate sonic boom prediction with meshes composed of "only" 2 millions vertices.

This adaptive procedure can be integrated in a three-stage modeling using the multi-pole reconstruction. Indeed, the multi-pole approach reduces the matching distance by taking into account crossflow effects. The adaptive CFD is then able to provide an accurate and certified mid-field signal (at a reduced matching distance) all around the aircraft. Moreover, this approach give another possible way to certify that there is no more non-linearities and to ensure that the coupling is valid. With this coupling, we can envisage to match mid-field CFD signals with the mid-field signals resulting from the propagation of near-field entries.

Acknowledgments

This work was partly supported by EC DG-XIII under HISAC project.
Dassault-Aviation is gratefully acknowledged for providing the three SSBJ configurations.

References

[1] F. Alauzet. Size gradation control of anisotropic meshes. *Finite Elements in Analysis and Design*, 2009. to appear.

[2] F. Alauzet, A. Loseille, A. Dervieux, and P.J. Frey. Multi-dimensional continuous metric for mesh adaptation. In *Proc. of 15th Int. Meshing Rountable*, pages 191–214. Springer, 2006.

[3] P. Batten, N. Clarke, C. Lambert, and D.M. Causon. On the choice of wavespeeds for the HLLC riemann solver. *SIAM J. Sci. Comput.*, 18(6):1553–1570, 1997.

[4] H.W. Carlson. Simplified sonic-boom prediction. TP. 1122, Nasa, 1978.

[5] H.W. Carlson, R.J. Mack, and O.A. Morris. A wind-tunnel investigation of the effect of body shape on sonic-boom pressure distributions. TN. D-3106, Nasa, 1965.

[6] M.J. Castro-Diaz, F. Hecht, B. Mohammadi, and O. Pironneau. Anisotropic unstructured mesh adaptation for flow simulations. *Int. J. Numer. Meth. Fluids*, 25:475–491, 1997.

[7] Ph. Clément. Approximation by finite element functions using local regularization. *Revue Française d'Automatique, Informatique et Recherche Opérationnelle*, R-2:77–84, 1975.

[8] P.-H. Cournède, B. Koobus, and A. Dervieux. Positivity statements for a Mixed-Element-Volume scheme on fixed and moving grids. *European Journal of Computational Mechanics*, 15(7-8):767–798, 2006.

[9] C. Debiez and A. Dervieux. Mixed-Element-Volume MUSCL methods with weak viscosity for steady and unsteady flow calculations. *Computer & Fluids*, 29:89–118, 2000.

[10] A. Dervieux, D. Leservoisier, P.-L. George, and Y. Coudiere. About theoretical and practical impact of mesh adaptations on approximation of functions and of solution of PDE. *Int. J. Numer. Meth. Fluids*, 43:507–516, 2003.

[11] C. Dobrzynski and P.J. Frey. Anisotropic delaunay mesh adaptation for unsteady simulations. In *Proc. of 17th Int. Meshing Rountable*, pages 177–194. Springer, 2008.

[12] P.J. Frey and F. Alauzet. Anisotropic mesh adaptation for CFD computations. *Comput. Methods Appl. Mech. Engrg.*, 194(48-49):5068–5082, 2005.

[13] P.J. Frey and P.-L. George. *Mesh generation. Application to finite elements*. ISTE Ltd and John Wiley & Sons, 2nd edition, 2008.

[14] A.R. George. Reduction of sonic boom by azimuthal redistribution of overpressure. *AIAA Journal*, 7(2):291–298, 1969.

[15] P.-L. George. Tet meshing: construction, optimization and adaptation. In *Proc. of 8th Int. Meshing Rountable*, South Lake Tao, CA, USA, 1999.

[16] C. Gruau and T. Coupez. 3D tetrahedral, unstructured and anisotropic mesh generation with adaptation to natural and multidomain metric. *Comput. Methods Appl. Mech. Engrg.*, 194(48-49):4951–4976, 2005.

[17] W.D. Hayes, R.C. Haefeli, and H.E. Kulsrud. Sonic boom propagation in a stratified atmosphere with computer program. TN. CR-1299, Nasa, 1969.

[18] N. Héron, F. Coulouvrat, F. Dagrau, G. Rogé, and Z. Johan. Hisac midterm overview of sonic boom issues. In *Proc. of the 19th international congress on acoustics-ICA*, Madrid, Spain, 2007.

[19] D.C. Howe, K.A. Waithe, and E.A. Haering. Quiet spike near field flight test pressure measurement with computational fluid dynamics comparisons. *AIAA paper*, 2008-128, 2008.

[20] ICAO. *Manual of the ICAO Standard Atmosphere (extended to 80 kilometres)*. Doc 7488. Third edition edition, 1993.

[21] W.T. Jones, E.J. Nielsen, and M.A. Park. Validation of 3d adjoint based error estimation and mesh adaptation for sonic boom reduction. *AIAA paper*, 2006-1150, 2006.

[22] B. Van Leer. Towards the ultimate conservative difference scheme i. The quest of monotonicity. *Lecture notes in physics*, 18:163, 1972.

[23] X. Li, M.S. Shephard, and M.W. Beal. 3D anisotropic mesh adaptation by mesh modification. *Comput. Methods Appl. Mech. Engrg.*, 194(48-49):4915–4950, 2005.

[24] A. Loseille. *Adaptation de maillage anisotrope 3D multi-échelles et ciblée à une fonctionnelle pour la mécanique des fluides. Application à la prédiction haute-fidélité du bang sonique*. PhD thesis, Université Pierre et Marie Curie, Paris VI, Paris, France, 2008. (in French).

[25] A. Loseille, A. Dervieux, P.J. Frey, and F. Alauzet. Achievement of global second-order mesh convergence for discontinuous flows with adapted unstructured meshes. *AIAA paper*, 2007-4186, 2007.

[26] J.M. Morgenstern, A. Arslan, V. Lyman, and J. Vadyak. F-5 shaped sonic boom demonstrator's persistence of boom shaping reduction through turbulence. *AIAA paper*, 2005-0012, 2005.

[27] J.A. Page and K.J. Plotkin. An efficient method for incorporating computational fluid dynamics into sonic boom prediction. *AIAA paper*, 1991-3275, 1991.

[28] C.C Pain, A.P. Humpleby, C.R.E. de Oliveira, and A.J.H. Goddard. Tetrahedral mesh optimisation and adaptivity for steady-state and transient finite element calculations. *Comput. Methods Appl. Mech. Engrg.*, 190:3771–3796, 2001.

[29] Pederson. Sonic boom technologies and challenges. In *FAA Civil Supersonic Aircraft Workshop*, Arlington, VI, USA, 2003.

[30] K.J. Plotkin. Theoretical basis for the finite difference extrapolation of sonic boom signatures. In *NASA Conference publication 3335*, volume 1, pages 54–67, 1995.

[31] K.J. Plotkin and J.A. Page. Extrapolation of sonic boom signatures from cfd solutions. *AIAA paper*, 2002-0922, 2002.

[32] P. Roe. Approximate Riemann solvers, parameter vectors, and difference schemes. *J. Comp. Phys.*, 43:357–372, 1981.

[33] C.W. Shu and S. Osher. Efficient implementation of essentially non-oscillatory shock-capturing schemes. *J. Comput. Phys.*, 77:439–471, 1988.

[34] R.J. Spiteri and S.J. Ruuth. A new class of optimal high-order strong-stability-preserving time discretization methods. *SIAM J. Numer. Anal.*, 40(2):469–491, 2002.

[35] J.L. Steger and R.F. Warming. Flux vector splitting of the inviscid gasdynamic equations with application to finite-difference methods. *J. Comput. Phys.*, 40:263–293, 1981.

[36] A. Tam, D. Ait-Ali-Yahia, M.P. Robichaud, M. Moore, V. Kozel, and W.G. Habashi. Anisotropic mesh adaptation for 3D flows on structured and unstructured grids. *Comput. Methods Appl. Mech. Engrg.*, 189:1205–1230, 2000.

[37] Ch. Thomas. Extrapolation of sonic boom pressure signatures by the waveform parameter method. TN. D-6832, Nasa, 1972.

[38] K.A. Waithe. Application of USM3D for sonic boom prediction by utilizing a hybrid procedure. *AIAA paper*, 2008-129, 2008.

Unité de recherche INRIA Rocquencourt
Domaine de Voluceau - Rocquencourt - BP 105 - 78153 Le Chesnay Cedex (France)

Unité de recherche INRIA Futurs : Parc Club Orsay Université - ZAC des Vignes
4, rue Jacques Monod - 91893 ORSAY Cedex (France)
Unité de recherche INRIA Lorraine : LORIA, Technopôle de Nancy-Brabois - Campus scientifique
615, rue du Jardin Botanique - BP 101 - 54602 Villers-lès-Nancy Cedex (France)
Unité de recherche INRIA Rennes : IRISA, Campus universitaire de Beaulieu - 35042 Rennes Cedex (France)
Unité de recherche INRIA Rhône-Alpes : 655, avenue de l'Europe - 38334 Montbonnot Saint-Ismier (France)
Unité de recherche INRIA Sophia Antipolis : 2004, route des Lucioles - BP 93 - 06902 Sophia Antipolis Cedex (France)

Éditeur
INRIA - Domaine de Voluceau - Rocquencourt, BP 105 - 78153 Le Chesnay Cedex (France)
http://www.inria.fr
ISSN 0249-6399